

2

AD-A265 959

PL-TR-93-2034



**WAVE PROPAGATION CHARACTERISTICS OF
SHORT-PERIOD CRUSTAL PHASES NEAR
ARCESS AND NORESS**

**Kristin S. Vogfjord
Charles A. Langston**

**Pennsylvania State University
Department of Geosciences
503 Deike Building
University Park, PA 16802**

February 1993

**Final Report
1 May 1991-31 October 1992**

**DTIC
ELECTE
JUN 03 1993
S E D**

APPROVED FOR PUBLIC RELEASE; DISTRIBUTION UNLIMITED



**PHILLIPS LABORATORY
Directorate of Geophysics
AIR FORCE MATERIEL COMMAND
HANSCOM AIR FORCE BASE, MA 01731-3010**

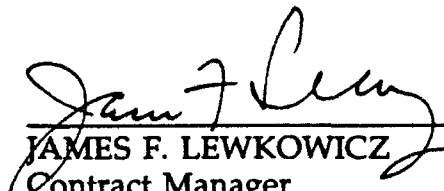
93 0 00 036


93-12441



The views and conclusions contained in this document are those of the authors and should not be interpreted as representing the official policies, either express or implied, of the Air Force or the U.S. Government.

This technical report has been reviewed and is approved for publication.


JAMES F. LEWKOWICZ
Contract Manager
Solid Earth Geophysics Branch
Earth Sciences Division


JAMES F. LEWKOWICZ
Branch Chief
Solid Earth Geophysics Branch
Earth Sciences Division


DONALD H. ECKHARDT, Director
Earth Sciences Division

This report has been reviewed by the ESD Public Affairs Office (PA) and is releasable to the National Technical Information Service (NTIS).

Qualified requestors may obtain additional copies from the Defense Technical Information Center. All others should apply to the National Technical Information Service.

If your address has changed, or if you wish to be removed from the mailing list, or if the addressee is no longer employed by your organization, please notify PL/IMA, 29 Randolph Road, Hanscom AFB, MA 01731-3010. This will assist us in maintaining a current mailing list.

Do not return copies of this report unless contractual obligations or notices on a specific document requires that it be returned.

REPORT DOCUMENTATION PAGE			Form Approved OMB No 0704-0188	
Public reporting burden for this collection of information is estimated to average 1 hour per response, including the time for reviewing instructions, searching existing data sources, gathering and maintaining the data needed, and completing and reviewing the collection of information. Send comments regarding this burden estimate or any other aspect of this collection of information, including suggestions for reducing this burden, to Washington Headquarters Services, Directorate for Information Operations and Reports, 1215 Jefferson Davis Highway, Suite 1204, Arlington, VA 22202-4302, and to the Office of Management and Budget, Paperwork Reduction Project (0704-0188), Washington, DC 20503.				
1. AGENCY USE ONLY (Leave blank)		2. REPORT DATE February 1993		3. REPORT TYPE AND DATES COVERED FINAL - 5/1/91 - 10/31/92
4. TITLE AND SUBTITLE Wave Propagation Characteristics of Short-Period Crustal Phases Near ARCESS and NORESS			5. FUNDING NUMBERS PE 62101F PR 7600 LA 09 WU AQ Contract F19628-90-K-0044	
6. AUTHOR(S) Kristin S. Vogfjord Charles A. Langston				
7. PERFORMING ORGANIZATION NAME(S) AND ADDRESS(ES) Pennsylvania State University Department of Geosciences 503 Deike Building University Park, PA 16802			8. PERFORMING ORGANIZATION REPORT NUMBER	
9. SPONSORING/MONITORING AGENCY NAME(S) AND ADDRESS(ES) Phillips Laboratory 29 Randolph Road Hanscom AFB, MA 01731-3010 Contract Manager: James Lewkowicz/GPEH			10. SPONSORING/MONITORING AGENCY REPORT NUMBER PL-TR-93-2034	
11. SUPPLEMENTARY NOTES				
12a. DISTRIBUTION/AVAILABILITY STATEMENT Approved for Public Release, Distribution Unlimited			12b. DISTRIBUTION CODE	
13. ABSTRACT (Maximum 200 words) Wave propagation of crustal phases near the ARCESS array is examined and compared to characteristics near the NORESS array, with emphasis on Lg and its composition. 1-k analysis is applied to the data, to identify arrivals in the records, then a composite of array beams is used to approximate each event. Record sections of composite-seismograms are constructed for different directions from ARCESS, to study propagational characteristics with distance and azimuth. Near surface velocity under NORESS and ARCESS is obtained through inversion of Rg wave dispersion curves. A composite ARCESS record section is compared to a NORESS record section of events located in the Caledonides. The differences that emerge are that Lg in the Caledonian region, north of NORESS, is dominated by discrete arrivals representing Moho reflections, with the order of reflection increasing with distance. In the Archean ARCESS region, however Lg is dominated by turning waves, also with the order of reverberation increasing with distance, but with each confined to a small distance range. Rg wave propagation in the ARCESS region is much more efficient than in the Caledonian NORESS region, as Rg is observed to 400 km distance at ARCESS, but only to 200 km distance at NORESS. Synthetic record sections are constructed by wavenumber integration, in order to model the observed character of Lg and Rg in the two regions. The dominating factor in the difference of Lg characteristics, turns out to be the velocity gradient in the lower crust. A few earthquakes near ARCESS are also studied. Their depths can be constrained on the basis of phase velocities and depth phases. For reliable phase identification, however, the composition of Lg in the region needs to be accurately known.				
14. SUBJECT TERMS ARCESS, NORESS Regional Wave Propagation, Rg -Wave Phase-Velocity Inversion for S-Wave Velocity			15. NUMBER OF PAGES 54	
			16. PRICE CODE	
17. SECURITY CLASSIFICATION OF REPORT Unclassified	18. SECURITY CLASSIFICATION OF THIS PAGE Unclassified	19. SECURITY CLASSIFICATION OF ABSTRACT Unclassified	20. LIMITATION OF ABSTRACT SAR	

Table of Contents

List of Scientist Contributing to this Report	iv
List of Previous Contracts Related to this Research	iv
Report Summary	iv
Task Objectives	iv
Technical Problem	iv
General Methodology	iv
Technical Results	v
Important Findings and Conclusions	v
Significant Hardware Development	vi
Special Comments	vi
Implications for Further Research	vi
Introduction	1
N-E Profile	4
E Profile	5
S-E Profile	8
S-W Profile	9
Earthquakes	11
R _g waves	13
Discussion and Conclusions	14
References	19

ACTE 001-100-1000 3

Accession For	
NTIS CRA&I	<input checked="" type="checkbox"/>
DTIC TAB	<input type="checkbox"/>
Unannounced	<input type="checkbox"/>
Justification	
By	
Distribution /	
Availability Codes	
Dist	Avail and/or Special
A-1	

List of Scientist Contributing to this Report

Charles A. Langston, P. I.

Kristin Vogfjörð, Research Assistant

List of Previous Contracts Related to this Research

Wave Propagation at Regional Distances, Contract # F19628-89-K-0013

Report Summary

Task Objectives

Characterization of local and regional wave propagation in the crust and upper mantle around the short-period arrays, NORESS and ARCESS.

Technical Problem

A condition for short-period, small-aperture arrays, which are key to reliable regional nuclear test monitoring, to be reliable, is proper knowledge of the regional wave propagation. In particular, the composition of *Lg* and how it varies with distance and azimuth. This will ensure accurate phase identification and possibly enable detection of depth phases, resulting in accurate distance and depth locations. Distance mislocations by IMS of local and regional events at NORESS and ARCESS mainly occur as a result of missed small amplitude *Pn* arrivals at NORESS and due to misidentified onset of *Lg* at both arrays as a result of improper knowledge about *Lg* wave propagation. Backazimuth mislocations occur due to insufficient knowledge about the location of crustal heterogeneities and Moho undulations, which cause multipathing near the arrays.

General Methodology

f-k analysis is applied in sliding time-windows to detect phases and determine phase velocities and azimuth of approach. Composite seismograms for events are made from time pieces of array beams, with each time section representing an arrival. Composite-seismogram record sections are

constructed and compared to synthetic seismograms calculated by wavenumber integration in plane-layered velocity models

Phase-velocity dispersion curves of *Rg* waves are inverted for near-surface shear-wave velocity under ARCESS and NORESS.

Technical Results

Important Findings and Conclusions

Lateral variations in crustal structure near ARCESS are apparent from the observations: A westward dipping Moho 75 km NE of ARCESS causes an approximately 8° backazimuth mislocations of events from Varanger Peninsula; lateral velocity changes cause a 13° backazimuth mislocation of a high frequency event from the Nikel mine; low phase velocities in the *Lg* wave train from easterly azimuth may be indicative of scattering east of the array; off-azimuth arrivals in *Pn* from events SW of ARCESS are probably caused by upper mantle heterogeneities.

Rg propagates efficiently out to at least 400 km in the ARCESS region, with a group velocity of 3.0 km/s in the region east of ARCESS, and 2.8 km/s in the region SW of the array.

Amplitude-maximums in the *Lg* wave train can be explained in terms of arrivals of rays, in order to simplify the interpretation and to understand the distribution of the wave energy in the crust. From such simple interpretation of the composite record-sections and through synthetic seismogram calculations it is concluded that *Lg* is dominated by turning waves with each order of reverberation dominating over a short distance interval until the next higher order takes over.

Depth phases of events studied are small and can only be accurately identified and thus used to extract source depth if the travel-time curves and amplitude pattern of the crustal phases are accurately known.

The wave propagation pattern at ARCESS is significantly different from that at NORESS. Upper mantle waves are of larger amplitude at ARCESS and are easily detected. *Lg* also has a strikingly different character: At NORESS the *Lg* wave train is dominated by discrete arrivals representing Moho reflections. Each order of reflection is sustained over a distance range of approximately 300 km, so that at some distances more than one reflection is of significant amplitude. The dominance of turning waves at ARCESS causes each

reverberation to be concentrated over a smaller distance range (approximately 150 km), so usually only one dominates the *Lg* wave train. Common to both regions, however, is that as distance increases, the first apparent arrival in the *Lg* wave train is of successively higher order multiple.

Significant Hardware Development

N/A

Special Comments

N/A

Implications for Future Research

The difference in character of *Lg* in the NORESS and ARCESS regions demonstrates the necessity to perform a similar study for other regional arrays, to extract the propagational characteristics of *Lg* in each region. This is a precondition for accurate phase identification and possible depth discrimination with a regional array.

Introduction

A regional seismic array provides a unique opportunity in event location and discrimination, in that it allows the determination of phase velocity as well as backazimuth of each phase detected from a seismic event. As a result, if velocity structure is adequately known, the travel path of each arrival can be determined. Repeated explosions in known mines provide the basis for building knowledge about the phases that dominate at local and regional distances, and how their amplitudes and travel times vary with distance and azimuth. As more events in a specific region are studied the characteristics of the regional wave propagation emerge and any additional arrivals, such as depth phases can be accurately identified to reveal source depth. The *Lg* wave train is of particular interest since it is usually the largest wave on local and regional seismograms and can propagate to great distances. It is composed of waves trapped in the crust, turning and multiply reflecting off the Moho, with the order of multiple increasing with distance. The *crustal P* wave train, on the other hand leaks its energy into the mantle, by mode conversion and therefore does not propagate efficiently.

In a previous study we obtained the characteristics of wave propagation near the NORESS seismic array in southern Norway (Vogfjrd and Langston, 1990; Vogfjrd, 1991). In this paper we report the results of a similar study of wave propagation near the ARCESS array in northern Scandinavia, with emphasis on *Lg*. Location of the ARCESS array and the structural units of the northern and central part of the Baltic shield are shown in Figure 1. The age of the Baltic shield decreases from Archean in the northeast, to Proterozoic in the center and southwest. It is built up by crustal accretion to the southwest by subsequently younger Proterozoic orogenies. Along the western margin runs the younger Caledonian Province (Gal and Gorbatshev, 1987). In the region east of ARCESS, the Pechenga-Varzuga belt separates two Archean blocks and marks the suture of a continent-continent collision that took place during the early Proterozoic. Later in the Proterozoic this suture was offset by the N-S striking North Karelian Megashear (dashed in Figure 1). As a result of the continental collision a slice comprised of metasediments and continental crust was thrust over the Archean basement to the south. This overthrust wedge forms the Lapland Granulite Belt and the Inari Terrain (Berthelsen and Marker, 1986; Gal et al., 1989).

The most detailed refraction profiles crossing the region of study are the FENNOLORA profile, which runs just west of ARCESS (Galson and Mueller, 1986; Guggisberg and Berthelsen, 1987; Guggisberg et al., 1991; Lund, 1987) (Figure 1) and the POLAR Profile, which runs just east of ARCESS and crosses the Granulite belt and the PV suture (Luosto et al, 1989). Other profiles include FINLAP, which extends east from FENNOLORA (Luosto et al, 1983) and profiles in Russia (Azbel et al., 1989; Glaznev et al., 1989). Crustal thickness on POLAR varies between 40 and 47 km, being thinnest under the center of the profile. A northward dipping wedge of higher velocities was found in the upper crust where the profile crosses the Granulite Belt and rather low velocities (6.8-6.9 km/s) were obtained for the lower crust in the center of the profile (Luosto et al, 1989; Behrens et al., 1989). Figure 2a shows the average velocity function under the northern end of the POLAR Profile. Near ARCESS the crustal thickness on FENNOLORA is around 45 km and near the intersection of FENNOLORA with FINLAP the structure consists of intermittent high and low velocity layers in the upper crust (Guggisberg et al., 1991). This is also the part of FENNOLORA that runs along the Baltic Bothnian megashear, a vertical shear zone extending through the crust (Berthelsen and Marker, 1986). The velocity profile in Figure 2b represents the velocity on FENNOLORA just north of the intersection with FINLAP. Crustal thickness obtained under FINLAP is 49 km (Luosto et al, 1983). Interpretation of refraction profiles that cross the Kola Peninsula has revealed a 10 km deep high-velocity region under the eastern end of the Granulite Belt and a crustal thickness varying from 36 km under northeastern Kola peninsula to 44 km under the southwestern Peninsula (Azbel et al., 1989; Glaznev et al., 1989). The velocity profile obtained in the Kola superdeep drillhole, which penetrates the Pechenga Belt, near the Nickel mine (Figure 1) shows higher velocities in the upper, 6.8 km thick, Proterozoic section than in the Archean basement below (Kozlovsky, 1987). The effects of this higher velocity in the suture zone may be the cause for multipathing observed in one event from Nickel. The effects of Moho undulations are also observed in a few events.

The dataset consists of 29 events from the IMS database, at distances between 60 and 583 km from ARCESS, representing 16 locations. Three of the events are identified as earthquakes. The azimuthal distribution is between 30° and 250° and magnitudes are between 1.8 and 3.2. Events are listed in Table 1 and their distribution is shown in Figure 1. IMS locations are shown by

triangles on the map and relocated positions, which in some cases coincide with known mines, are indicated by solid circles. Distance mislocations by TMS are caused by missed onset of *Lg*, while backazimuth mislocations are caused by Moho undulations and/or lateral velocity gradients, causing variations in backazimuth between the different phases of an event. Backazimuth mislocations are most prominent for mine explosions on the Varanger Peninsula, northeast of the array, for an explosion in the Nikel mine, east of the array and for an explosion southwest of the array, in the vicinity of the Malmberget mine. Three events are located in the Caledonian region northeast of the array, the four most westerly events, near Kiruna and Malmberget mines, are in the Proterozoic region and the rest is located in Archean crust.

Coherent arrivals in the data are detected and identified with f-k analysis in sliding time windows, beams are formed for the major phases and a composite seismogram for each event is then made from time sections of the beams. In this form the data is used to construct record sections in order to study the characteristics of regional wave propagation in the ARCESS region.

Phase-velocity dispersion curves of *Rg* waves from 12 of the events are used to obtain the near-surface shear velocity under the ARCESS array and *Rg* waves from 11 additional events (Table 2) recorded at NORESS are used to obtain the near-surface velocity structure under that array as well.

The composite seismograms are plotted on four record sections, based on backazimuth range, in order to observe and model the phase behavior with distance and backazimuth. The pattern that emerges puts constraints on lower crustal and upper mantle velocity structure. As expected the *crustal P* wave train quickly diminishes with distance, while arrivals in the *Lg* wave train remain large over the 600 km distance range studied. A synthetic record section is constructed to model the phase behavior observed in *Lg*. Calculations are done by wavenumber integration in the plane-layered velocity model of Figure 2a, which is based on the average velocity obtained for the northern part of POLAR (Luosto et al., 1989). The Q model used is also shown in Figure 2a. For a comparison with the characteristics of wave propagation in southern Norway a composite record section from NORESS is also shown and a synthetic record section, calculated using the Caledon velocity and Q model shown in Figure 2c. The model is based on upper crustal velocities of the Precambrian model of Gundem (1984) and the lower crustal model obtained for the Arsund-

Otta refraction profile (Mykkeltveit, 1980). The Q_s models used are constrained in the top 3 km of the crust by the observed R_g wave attenuation in the region. The Q -values used for the middle and lower crust are needed for efficient I_g wave propagation, but are otherwise not constrained. From the comparison of record sections, it is concluded that wave propagation in the Archean Baltic shield is governed mostly by velocity gradients in the lower crust and upper Mantle, as well as by the Moho discontinuity. In southern Norway, on the other hand the gradients are small and the Moho discontinuity has the greatest effect on the regional wave propagation, giving rise to reflections, which can be traced over greater distances than those in the north.

After having established the propagational characteristics of the ARCESS region, three events can be identified as earthquakes. Their source depths is constrained by the timing and phase velocities of the observed phases, which in two events include depth phases

N-E Profile

Three events are located north of the array, 998975 and 1206599 in the same location on Varanger Peninsula and 1361299—a possible earthquake—near the northern tip of Nordkinn Peninsula. A composite record section with events from the two locations is shown in Figure 3, with event 1361299 high-pass filtered at 1 Hz to get rid of low-frequency noise. Superimposed on the plot are travel-time curves for the major phases expected from a near-surface source in a Polar velocity model with a 45-km thick crust. The 45 km crustal thickness is constrained by the PmP - P_g and SmS - S_g travel times of the events at 150 km distance. Slopes on the travel-time curves show what the expected phase velocities are for each phase at a particular distance. The slope can be read from the velocity template in the top center of the plot. Phase velocities obtained from the data by f-k analysis and used for beamforming, are indicated above the beam sections of the composite seismograms.

The two events on Varanger Peninsula are from a quartzite mine at 70.48N and 38.50E (Mykkeltveit, 1992 pers. comm.) and appear very similar. S waves of both events are dominated by 2.2 Hz frequencies. P phases, however, of event 989975 are dominated by 5.5 Hz waves, while event 1206599 is dominated by 9.1 Hz P_g waves and 7.4 Hz PmP waves. The phase velocity of the 2.2 Hz S_g is unusually low (3.3 km/s), which may be due to scattering near the array. The small amplitude of the phase, makes contamination by background

noise also a possible cause. Less energetic waves of higher frequencies, however (3.3 and 4.4 Hz) have the expected 3.6-4.0 km/s phase velocities. No *Rg* waves are found in the records from this mine. This is probably caused by propagation across the innermost section of the Tanafjord. Common to seismograms from the two events, is a difference in backazimuth between the crustal waves (*Pg*, *Sg*) and the Moho reflections (*PmP*, *SmS*). This can also be seen in Figure 3, where the broad-band power spectra for the four main phases of event 989975 are inset. The *Pg* phase has been band-pass filtered between 4.8 and 5.8 Hz and the *Sg* phase between 1.5 and 7.0 Hz. The backazimuths obtained for the crustal waves are between 46.3° and 48.9° (except for the higher frequency *Pg* of event 1206599, where it is 42.1°). The Moho reflections on the other hand have backazimuths between 52.3° and 54.9°. Comparing this to the true backazimuth of the mine, which is 45.9°, it is clear that the crustal waves give a backazimuth which is closer to the true backazimuth. To account for the difference between the crustal phases and the Moho reflections, a westward dip in the Moho is required at the point of reflection, 75 km northeast of ARCESS. The IMS locations, (shown by triangles in Figure 1) are mainly based on backazimuths of the Moho reflections, whose quality is much higher than that of the crustal waves i.e. amplitude is greater and range in backazimuth is smaller.

Due to its location, near the tip of Nordkinn Peninsula, event 1361299 could be an earthquake. The absence of *Rg* also supports that. The phase velocities obtained for the first arriving P and S waves however indicate crustal waves, *Pg* and *Sg*, constraining the source depth to be in the top 5 kilometers below the surface; greater source depths would cause *Pn* and *Sn* to be the first arriving phases. All the energy in this event is limited to the 3-5 Hz band, with energy peaking at 4 Hz. This may be indicative of an explosion, however maximum amplitude on the tangential component is roughly twice that on the vertical which conversely may be indicative of an earthquake. The nature of this event can therefore not be determined.

E Profile

Four locations are represented by the events on this profile, as shown in Figure 4. Two locations are known mines: the Sydvaranger mine at 69.652N 30.025E and the Nikel mine at 69.409N 30.955E. The other two events, despite the absence of *Rg* waves, are probably from near-surface sources also; they

are fairly well matched by surface-source travel-time curves and their locations coincide with many other events. Travel-time curves for the major phases in a Polar velocity model are superimposed. A 42 km thick crustal model fits the arrival times in the data, however thickness is not well constrained. The Moho reflections for the three closest events occur in a region near the POLAR Profile, where crustal thickness varies between 41 and 45 km (Luosto et al., 1989). R_g waves on this profile move out with a group velocity of 3.0 km/s.

Even though events from the Sydvaranger mine have P_g arriving ahead of PmP , explosion practice at the mine prevents the resolution of crustal thickness from PmP - P_g time. This is demonstrated in Figure 5a, where four events from Sydvaranger are plotted, aligned on the first arrival. Following are sequences of arrivals, depending on the multiplicity of the explosion. This is particularly clear in event 460928, which demonstrates multiple discrete arrivals, with varying phase velocities. The first arrival has a dominating phase velocity around 7 km/s, representing diving waves turning in the lower crust. The last P arrival, with a dominating phase velocity around 8.7 km/s represents the Moho reflection, PmP . The apparent velocity of 8.1 km/s obtained for the intermediate arrival is probably due to interference between PmP and P_g because of the multiple source. The source multiplicity is also seen in the S waves and can be inferred from the interference patterns in some of the R_g waves. From the slopes on the travel-time curves for PmP and SmS , the expected phase velocities are 7.5 and 4.3 km/s, respectively. The high phase velocities obtained for the Moho reflections from Sydvaranger, therefore indicate a westward dipping Moho at the point of reflection. Backazimuths obtained for the different phases are close to the true backazimuth of the mine.

The five events shown in Figure 5b are from the Nikel mine. They have been stacked with phase velocities of the Moho reflections, PmP and SmS , and the surface wave R_g . Except for 326360a and 282554, the events appear to consist of multiple explosions. Expected first arrival from this distance (see Figure 4) is the upper mantle Pn wave, followed by P_g and PmP . The apparent velocity in the first 0.5 s, however represents crustal waves so Pn amplitudes must be small. Moho reflections have the largest amplitude at this distance and, except for event 326360, they are dominated by low frequencies, 2-3 Hz. Event 326360 starts off with 2.2 Hz and the same phase velocity as in the other

events, but then higher frequency waves, 7 and 10 Hz, take over, and phase velocity increases. Except for these high frequency waves, backazimuth range obtained for the different phases is close to the true backazimuth of 91.2° , or $92.8-93.8^\circ$ for P waves and $93.1-98.4^\circ$ for S waves. The backazimuth of the high-frequency P arrivals on the other hand is 105° . The higher frequency waves therefore have traveled a different path to the array. This effect is not seen in events from the Sydvaranger mine. Location of the Nikel mine, in the Pechenga belt and close to the Kola superdeep borehole, where velocities in the Proterozoic top 6 km are greater than in the Archean basement below (Kozlovsky, 1987), suggests that the high-frequency waves experience lateral velocity gradients within the Pechenga belt, which do not affect the lower frequencies.

Even though event 348962, at 245 km distance, apparently lacks an *R_g* wave (Figure 4) it is probably an explosion. It is followed approximately one minute later by a near identical event and the vertical and tangential components are approximately equal in amplitude. This event is dominated by 3 Hz waves, it has no detectable *S_n* wave and an unusually low phase velocity, 3.4 km/s, dominates the S waves. The expected 4.2 km/s phase velocity of *S_mS* is obtained in the frequency band around 6 Hz, but the energy is only 1/5 of the energy of the 3 Hz waves. Due to the small amplitudes in this event *R_g* may be overshadowed by the low-frequency background noise.

At 350 km distance, in event 335253, the second Moho reflection has become prominent, while the first reflection has decreased in amplitude (see Figure 4) a pattern seen in other events in the region east and southeast of ARCESS. *PmP* is not detected, but *S_mS* still is, with the appropriate phase velocity. Its amplitude however, is smaller than that of *2xS_mS*. Most arrivals are dominated by 3-4 Hz waves and backazimuths for most phases are between 87° and 92° , except for the second order reverberations where backazimuth is around 100° . This may be caused by the surface reflection occurring in the Pechenga belt near Nikel. The arrivals can be matched with travel-time curves for a surface source and the absence of *R_g* can be explained by passage across a sea channel near the source region.

Missed onset of *L_g* by the IMS system causes distance mislocations of events on this profile, and multipathing probably due to lateral velocity gradients causes backazimuth mislocations of high frequency events at Nikel. The IMS time picks for *P_n* and *L_g* are indicated by arrows on Figure 5, showing

many missed onsets of *Lg*. For example, in event 760713 *Rg* is misidentified as *Lg*. Event 335253, at 350 km distance was also mislocated due to missed *Sn* and *SnS* arrivals. The IMS time pick for *Lg* in event 335253 is indicated by an arrow at 59 sec in Figure 4.

S-E Profile

Events from four locations south-east of ARCESS are plotted in Figure 6 with travel-time curves for a 45 km thick crust. Over the distance range shown, *Pn*, *Sn*, *2xSg* and *3xSg* dominate the seismograms. *2xPnP* and *2xSmS* are detected out to 400 km distance, while *PnP* and *SnS* have disappeared. *Rg*, with a group velocity of 3.0 km/s is observed out to 400 km distance.

Comparing event 1350700, at 350 km distance, with event 335253, at 350 km distance on the record section due east (Figure 4), it is apparent that the *Lg* wave train between 50 and 63 sec in event 1350700 is much more complex than *Lg* in the same time window of event 335253: At 52 s and 56 s, arrivals with 4.6 km/s and 5.2 km/s phase velocity, respectively, interfere with the expected *Sg* *2xSg* arrivals, which have phase velocities around 3.8 km/s. In event 335253, only the *2xSg* arrivals with the expected phase velocity of 3.9 km/s are seen in this time window. A possible explanation is a second, delayed explosion, so that the alternating high and low velocities in the *Lg* wave train are caused by interference between *Sn*, *2xSg* and *2xSmS* from the two sources. The arrival at 30 seconds is probably *2xPnP-PmS*, rather than the third *Pn*, since there is no corresponding *S* arrival at 67 seconds. The extended duration of the *Rg* wave is also indicative of a double explosion. Except for *Rg*, all the phases of event 1350700 are dominated by 5 Hz waves, and backazimuth obtained for the upper mantle waves is 119°, while the crustal waves have backazimuths near 110°.

Event 329174 is from one of the mines near Apatity, which have backazimuths between 117.36° and 118.12°. The location plotted in Figure 1 corresponds to the Koashva mine at 67.64N 34.02E. Backazimuths obtained for the different phases of the event are mostly between 117° and 119°. The dominating phases at this distance are *2xSg*, *3xSg*, *2xSmS*, *Pn* and *Sn*. *Rg* is also of significant amplitude. A second smaller event studied, from the Apatity area has similar phase velocities and backazimuths, but a *Pn* amplitude comparable to that of *2xSmS*. Probably due to its smaller size however, it has no detectable *Rg* wave.

Event 1143047 at 510 km distance is the largest event studied and therefore more multiple bounces are observed from it; possibly the fourth Moho reflection is detected in the crustal *P* wave train. Largest amplitudes, however are observed at the arrivals of the many branches of $3xSg$ (see Figure 6). The phase velocity of the dominating arrivals (3.5 km/s) is representative of these turning waves. An increase in amplitude and phase velocity, 10 s later coincides with the travel-time curve for $3xSmS$. The event is dominated by low-frequency waves, 2- 4 Hz and backazimuths of the various phases range between 135° and 140°. The large amplitudes of S waves as compared to those of P waves might suggest an earthquake source, but no depth phases are observed. SH amplitudes are only slightly larger (x1.4) than the vertical SV-waves. The amplitude difference between P and S waves can be entirely explained by the entrapment of shear waves in the crustal wave guide, while P waves continually lose some of their energy into the mantle, by mode conversion.

At 583 km distance, the upper mantle waves, Pn and Sn , in event 240323 have the largest amplitudes. The second multiples, $2xPn$ and $2xSn$ are also detected. The crustal P wave train has practically vanished, but $3xSg$ and $3xSmS$ are still observed. Phase velocities in the *Lg* wave train range between 3.0 and 4.4 km/s, with the lower phase velocities dominating, early on in the wave train, then phase velocities near 3.5 km/s become more energetic. The explanation for the low phase velocity (3.0 km/s) can be the dominance of turning waves in this region, in which case the low phase velocity means the waves have travelled in the upper crust. Alternatively it can be due to scattering in the vicinity of the array. *Rg* is not detected at this distance. Comparison with a second event obtained from this location, reveals that the small, low-frequency Pn precursor is probably the result of a double source rather than a structural effect. A phase velocity of 8.2 km/s dominates the Pn arrivals in event 240323. In the other event however, the main Pn arrival has a higher dominating velocity, 8.8 km/s. Backazimuths vary between 151 and 157°. The two events are associated with a mine location (SC17) at 64.685N 30.660E, with a backazimuth of 155.1°.

S-W Profile

South-west of ARCESS, the three events nearest to the array are earthquakes. Of the remaining three locations, one corresponds to a known

mine; at 286 km distance the Kiruna mine is located at 67.83°N 20.21°E (Figure 1). The Kiruna event is also the only one in this region with a detectable *R_g* wave. Its group velocity is 2.8 km/s, or lower than on the E and SE profiles. Figure 7 shows a record section with the three surface events and one of the earthquakes (at 261 km distance). Travel-time curves for the major phases in a 45 km thick FENNOLORA velocity model (Figure 2b) are superimposed. This is the velocity model obtained for the section of FENNOLORA just north of its intersection with the FINLAP profile (Figure 1). The earthquake, event 392876 at 261 km distance, is included on the record section to demonstrate that depth phases may be mistaken for higher order reverberations, i.e. *2xPmP*, when propagation characteristics are not known. From the other events on the record section it is clear that *2xPmP* has not attained large enough amplitude to be detected in this distance range. The sequence of three separate 7.0 km/s P-arrivals in event 392876 can not be an effect of a multiple explosion either, because it is not matched in the *L_g* wave train.

Backazimuths obtained for the Moho reflections of the Kiruna event vary somewhat from the true backazimuth of 231°. The upper mantle waves *P_n* and *S_n* and the low frequency tail of the *L_g* wave all have backazimuths around 232°, while *PmP* and the higher frequency (>3 Hz) *SmS* have backazimuths around 225°. The same pattern is also observed for the phases of event 905793, at 310 km distance. Thus the Moho between 145-155 km distance southwest of ARCESS dips southward and so causes the Moho reflections, *PmP* and *SmS*, to arrive off azimuth. Propagation paths from these two events cross the FENNOLORA profile approximately 50 km north of the intersection with FINLAP. At this location on FENNOLORA the upper crustal structure is complex, with intermittent high- and low-velocity layers and a velocity of only 6.95 km/s at the base of the crust (Figure 2b). This value is lower than the velocity south of the intersection, along the propagation path from events 1206482 and 309164 (distance=342 km, backazimuth=210°) (see Figure 1), where the velocity above the Moho is 7.2 km/s. *PmP* and *SmS* from this location therefore arrive earlier than predicted by the FENNOLORA travel-time curves.

The Moho reflections, *PmP* and *SmS*, are still large and the second reverberation is just starting to emerge at 342 km distance and 210° backazimuth (events 1206482 and 309164). At the 230° backazimuth however, the amplitude of the Moho reflections have already started to decrease near 310 km distance (event 905793), and *2xPg* and *2xSg* carry much of the energy

(see Figure 7). This may be indicative of a greater velocity gradient in the upper crust and a smaller velocity gradient in the lower crust along the 210° backazimuth travel path, causing more of the energy to reflect off the Moho. For comparison, at 350 km distance on the profile due east from ARCESS, the first Moho reflection has started to lose energy and the second reflection, $2sSmS$, dominates the Lg wave train (Figure 4).

Event 1206482 is mislocated in backazimuth to the vicinity of the Malmberget mine, which is at 67.18°N 20.67°E. This is due to off azimuth Pn arrivals at frequencies above 5.5 Hz. In both events 1206482 and 309164, backazimuth around 225° and high phase velocities, 8.6-9.2 km/s and 5.0 km/s are obtained for the Pn and Sn arrivals, respectively at frequencies > 5.5 Hz. The higher frequency waves also appear to arrive later than the lower frequencies. Lower frequencies in the Pn and Sn windows however have the correct backazimuth of 210°. Event 120682 is mislocated in backazimuth because 8.2 Hz frequencies dominate the Pn arrival. The cause of these double upper mantle arrivals is probably in the upper mantle. Interpretation of FENNOLOLA travel times by Guggisberg and Berthelsen (1987) shows a high velocity region (8.6 km/s) in the upper mantle along the southern half of the propagation path.

Earthquakes

Three events all in the southwestern quadrant, can be identified as earthquakes, based on depth phases and/or phase velocities. Event 580540 is at a distance of only 60 km from the array. The three-component composite seismograms, shown in Figure 8a have no undisputed depth phases. However, the phase velocities obtained, 7.2 and 4.2 km/s for Pg and Sg respectively, are too high for this to be a surface event: at 60 km distance in the Fennolora model, Pg has a phase velocity of 6.2 km/s. Allowing for a ± 0.2 km/s uncertainty in phase velocity, the source depth can be constrained between 26 and 32 km with closest match at 30 km depth. This depth range is the same for both the Fennolora and the Polar velocity models. Attempts to extract a source mechanism for this event proved unsuccessful. Synthetics were calculated for a source in both the Polar and the Fennolora velocity models, but it was impossible to simultaneously fit the amplitudes of the two components of Pg and the three components of Sg . This may be due to an unmodeled P-to-S conversion interfering with Sg on the vertical and radial components. Figure

8a shows a high frequency arrival at 20 sec on the vertical and radial components, which may be just such an arrival. Since it is not observed on the tangential component it must be created by mode conversion at a velocity discontinuity. The amplitude of this phase could not be reproduced in the synthetics. A three-component synthetic calculated for a vss source at 30 km depth in the Fennolora model is plotted in Figure 8b. Considering the complex velocity model obtained for Fennolora in this region it is probably nontrivial to model events in this region.

The source depth of event 981647 is constrained by depth phases and high phase velocities of the first arriving P and S waves. With a P-S time of 19.2 sec, an event can only have first arriving P_n if the source is located at depth. Travel times and phase velocities of the detected phases can be matched with the source at 32 km depth and a 45 km thick crust. This is shown in Figure 9a, where travel-time curves are superimposed on a vertical composite seismogram. A tangential composite (shifted in distance) is also plotted for comparison. Its amplitude is more than double the amplitude of the vertical component. Synthetic seismograms were calculated, for a source at 32 km depth and 180 km distance in the Polar and Fennolora models. The separation of P_n , P_g and PmP , seen in the data is better matched by Fennolora synthetics. This is due to the lower phase velocity (6.95 km/s) at the base of the crustal model. The vertical-component composite and synthetics for the three fundamental dislocation sources are shown on Figure 9b. A mechanism could not be constrained, because first motions of arrivals were difficult to determine. IMS was not able to separate the P_n and P_g arrivals of this event. It triggered 0.3 s into the P_n arrival and the phase velocity reported, 6.8 km/s, reflects that of the P_g arrival. sP_g was detected but not identified.

Due to a location close to the Kiruna mine, event 392876 was initially mistaken for an event from the mine, however as more events from the area were studied it became apparent that the two P arrivals following PmP are the depth phases, $pPmP$ and $sPmP$. The vertical and tangential composite seismograms for the event are plotted in Figure 10, both high-pass filtered at 2 Hz. Travel-time curves of the main phases from a source at 18 km depth in the Fennolora model are superimposed on the plot. Dominating phase velocities of 6.9 and 7.1 km/s, obtained for the two arrivals following PmP , correspond well with the slopes on the travel-time curves of $pPmP$ and $sPmP$, respectively. Following SmS in the Lg wave train however, 3.7 km/s phase velocities,

representative of *sSg*, are as energetic as those of *sSmS*. With the dominating phase velocities obtained for the depth phases so similar to those of the Moho reflections, separate beams were not formed for any of the depth phases. Backazimuths obtained for crustal phases vary between 223 and 228, while those of the upper mantle waves appear to be higher. Because of their small amplitudes however, they are not as reliable. This event was mislocated by IMS due to missed onset of *Pn* and misidentification of *PmP* as *Pn*, despite a low phase velocity of 7.25 km/s. Both *sPmP* and *sSg* were detected but not identified.

Rg Waves

F-k analysis of *Rg* waves from 11 events recorded at the NORESS array and 12 events recorded at the ARCESS array, was used to gather information about the near-surface shear-wave velocity under the arrays. Event locations are shown in Figure 11a and -b. The phase-velocity dispersion curves obtained are plotted in Figure 12 over the frequency range where power is > 1% of the maximum. Maximum amplitude occurs around 1 Hz. Higher frequencies are increasingly attenuated with source distance and the 3 km array-aperture, limits resolution to frequencies above 1 Hz. Also shown is the weighted mean dispersion-curve and standard deviation for each array, where each curve is weighted by the maximum amplitude of the *Rg* wave. The distance range of events recorded at NORESS is 22-83 km, with the events from within 45 km distance containing significant energy up to 2.3 Hz. Thus allowing resolution of velocity between 1 and 3 km below the surface. The mean dispersion curve is nearly flat between 1 and 2 Hz at a phase velocity of $2.94 \pm .12$ km/s. The apparent decrease in the phase velocity above 2 Hz is within the limits of one standard deviation.

The *Rg*-wave producing events near ARCESS are at distances of 175, 210 and 350 km from the array. Phase velocity can therefore only be obtained for frequencies up to 1.5 Hz, allowing resolution of velocities between 2 and 3 km below the surface. The mean phase-velocity at 1 Hz is $3.15 \pm .04$ km/s, increasing to $3.27 \pm .07$ km/s at 1.4 Hz. The increase is outside the limits of one standard deviation and may therefore indicate an increase in velocity as the surface is approached.

The mean dispersion curves for the 1-2.3 Hz frequency band at NORESS and the 0.7-1.5 Hz band at ARCESS were inverted for shear velocity. The top 2.5 km were resolved. The data and inversion results are shown in Figure 13. The

inversion fits a near straight line to the data thus obtaining a constant shear-velocity of 3.16 km/s under NORESS and 3.45 km/s under ARCESS. The ARCESS model has velocity increasing towards the surface, but the increase is within one standard deviation and therefore not significant.

Discussion and Conclusions

R_g waves propagate very efficiently, with a group velocity of 3.0 km/s, in the region due east and southeast of ARCESS, where R_g is observed from a distance of 400 km. Southwest of the array however, R_g is absent from all but the Kiruna event, at 286 km distance and group velocity is also lower, 2.8 km/s. This suggests greater attenuation near the surface and lower surface velocity at southwesterly backazimuths. The results from the R_g -wave inversion indicate a near-constant S-wave velocity, of 3.5 km/s in the top 2.5 km under the ARCESS array and a lower, but constant velocity of 3.16 km/s under NORESS.

Apart from the top 2.5 km of the crust under ARCESS, upper crustal structure near the array can not be resolved, as no good quality events are available from within 100 km distance. Velocity structure in the lower crust however, is resolved. In the Archean region east of the array, velocity in the lower crust is well described by the POLAR Profile model (Figure 2a), while the lower crust in the region southwest of the array is maybe better described with the FENNOLOLA model (Figure 2b). The difference between the lower crusts of the two models lies in the velocity gradient; the Polar model has a higher gradient. East of ARCESS the velocity gradient in the lower crust is large enough to cause each Moho reverberation to be concentrated over a limited distance range (150-200 km), with the first reverberation dominating out to 250 km distance (Figures 4 and 6). On the southwestern record section however, the first Moho reflection dominates to at least 340 km distance (Figure 7). The velocity gradient therefore is probably lower in the region southwest of the array.

Crustal thickness on the POLAR and FENNOLOLA refraction profiles varies between 40 and 47 km in the ARCESS region (Guggisberg et al., 1991; Luosto et al., 1989). Due to the distance range of the events studied, raypaths are largely horizontal, so crustal thickness is not well resolved, but arrival times of the main phases in most events can be approximately matched with crustal thickness between 42 and 45 km. Effects of undulations in the Moho

are seen in off-azimuth arrivals of PmP and SmS from Varanger Peninsula and from the Kiruna mine. High phase velocities of the Moho reflections from the Sydvaranger mine are also indicative of a dipping Moho. Off azimuth arrivals in Pn and Sn , from an event southwest of the array are probably caused by lateral variations in upper mantle velocity. Phase velocities dominating the Lg wave train from southeasterly azimuths are very low (3.0-3.5 km/s), indicating that a significant part of the energy propagates in the upper crust and possibly that the S-waves are scattered in the vicinity east of the array.

To compare propagational characteristics in the ARCESS region to that in the NORESS region, a combined record section of composite seismograms from events in the Archean region east of ARCESS, covering distances between 150 and 583 km, is plotted in Figure 14. Travel-time curves for a near-surface source in a 45 km thick Polar model are superimposed. Figure 15 shows a composite record section of NORESS events located in the Caledonian region northwest of that array, covering a distance range between 50 and 500 km. Travel-time curves for a near-surface source in a 36 km thick Caledon model are superimposed. The ARCESS record section shows each order of Moho reflection dominating over a short distance interval until the next higher order takes over. A large portion of the energy is also carried by waves turning in the crust. This is particularly clear in the Lg wave train which propagates much more efficiently than the *crustal-P* wave train; *crustal-P* can not sustain many bounces off the Moho, as some of the P-wave energy escapes into the mantle as SV-waves. In Lg the first Moho reflection, SmS , dominates out to approximately 300 km, then diminishes and the second order reflection and turning wave, $2xSmS$ and $2xSg$, dominate from 300 km to approximately 500 km distance, where $3xSg$ and $3xSmS$ take over and dominate Lg at 600 km distance. Compare this with the NORESS record section in Figure 15, where each reflection can be followed over a greater distance range and more than one order of reverberation is large at each distance. The first reflection is large out to 300 km, the second reflection from 250 km and further. At 500 km SmS has vanished and $2xSmS$, $3xSmS$ and $4xSmS$ dominate the seismogram. This adds considerable complexity to the Lg wave train, as compared to the Archean region at ARCESS. The propagation distance of Rg in the NORESS region is less than 200 km and the upper mantle waves, Pn and Sn , are of smaller amplitude than in the ARCESS region.

The *Lg* wave train at distances > 100 km is dominated by waves turning in the lower crust and reflecting off the Moho. The wave train is therefore most sensitive to the velocity structure of the lower crust. A gradient in the lower crust will turn a significant amount of the wave energy, thus lessening the amount that reflects off the Moho and concentrating the energy of each reverberation over a short distance interval. A constant-velocity lower crust lets all of the energy reflect off the Moho after the critical distance for each reverberation is reached. The difference in propagation characteristics between the ARCESS and NORESS regions, can be explained by the difference between the Polar and Caledon velocity models (Figure 2a and 2c). Their main difference lies in the velocity of the lower crust. The Polar model has a significant velocity gradient in the lower crust (0.024 /s), whereas the Caledon model has a constant velocity lower crust. Synthetic seismograms calculated for an explosion source at 0.1 km depth in the Polar and Caledon velocity and *Q* models are shown in Figures 16 and 17, respectively. The Polar record section has the same characteristics as the ARCESS record section, with each reverberation dominating over a short distance range where the next higher order reverberation takes over. A significant amount of the energy is also carried by the waves turning in the lower crust. In the Caledon record section each reflection can be traced over greater distances and a smaller amount of the energy is carried by the waves turning in the crust. At 600 km distance all four reflections can be observed in the *crustal P* and *Lg* wave trains. *Rg* propagates to only 150 km distance in the Caledon model due to the 0.3 km thick low-*Q* surface layer. This layer is only 0.1 km thick in the Polar model, which allows *Rg* to propagate to at least 600 km distance.

Amplitudes of upper mantle waves are larger on the ARCESS record section than on the NORESS profile (Figures 14 and 15). This can be due to a greater velocity gradient in the ARCESS region and/or higher *Q* values in the upper mantle. The Polar model has both a greater upper mantle velocity gradient and higher *Q* values in the upper mantle than does the Caledon model. This results in larger amplitude *P_n* and *S_n* waves on the Polar record section.

The *Q* structures of the Polar and Caledon crustal models are identical except for the thickness of the low *Q* surface layer, which in the Caledon model (0.3 km) limits the propagation distance of *Rg* to 200 km distance. A 0.1 km thickness in the Polar model allows *Rg* to propagate to at least 600 km. The upper mantle *Q* is also lower in the Caledon model. Despite the near-identical *Q*

values in the crust, the maximum-amplitude decay with distance of Lg is greater in the Caledon model as the energy is divided among the many Moho reflections (Figures 16 and 17) and moveout of the maximum amplitude is not constant. The energy in the Polar model, on the other hand, is carried by waves turning in the crust and the maximum amplitude moves out with a constant group velocity of 3.6 km/s. When estimating the apparent- Q from Lg waves, a correction factor for geometric spreading of an Airy phase, $\Lambda^{5.6}$, where Λ is the distance in km (Nuttli, 1973), is normally applied. Then amplitude is assumed to decay as $e^{-\alpha\Delta}$, where $\alpha = \frac{\pi f}{UQ}$, with f = frequency and U = group velocity at the maximum amplitude. The apparent Q -values obtained from the synthetics, by this method are, approximately 1000 for the Polar model and approximately 750 for the Caledon model (increasing the thickness of the low- Q surface layer in the Polar model to equal that of the Caledon model gives the same results). The apparent Q obtained from Lg , therefore appears to depend on velocity structure as well as the Q structure of the crust. The reason for the lower apparent Q of the Caledon model may be inappropriate assumption for geometric spreading when the velocity gradient in the lower crust is small and Lg is dominated by Moho reflections with varying group and phase velocities. A similar conclusion was reached by Bowman and Kennet (1991) after obtaining unreasonably low Q values from Lg waves in a region of Australia, where the Moho is replaced by a gradient-zone allowing leakage of Lg energy into the mantle.

The Q value obtained by Sereno et al, (1988) from Lg recorded at NORESS is $560f^{0.26}$, which corresponds to 600-800 for the frequency range of the synthetics. This was obtained for the fixed group-velocity range 3.0-3.6 km/s. However, from the NORESS record section (Figure 15) it is clear that the moveout of maximum amplitude in the 200-300 km distance range is close to 3.9 km/s. It can therefore be assumed that their analysis missed a significant amount of Lg energy from events in the region west of NORESS, where crustal thickness is near 36 km. The crustal thickness of the Caledon model in Figure 17 is 42 km, which gives maximum amplitude in Lg within the 3.0-3.6 km/s group velocity window.

The Lg wave has been the object of theoretical and observational study for some time (see Hansen et al., for a short review). Because of its observed waveform complexity, seen from single station data, the Lg wave has been

difficult to explain in detail. In practice, *Lg* is usually thought of as the superposition of higher mode Love and Rayleigh waves (e.g., Nuttli, 1973) with scattering due to crustal inhomogeneities producing added complexity (Baumgardt, 1990). Theoretical mode calculations show that mode theory can explain much of the character of the *Lg* wave for wave propagation in plane layered media. However, the superposition of normal modes is often difficult to understand since 10's of modes are needed to produce high frequency arrivals in the *Lg* wavetrain. We have shown that simple ray theory explanations of arrivals within the *Lg* wavetrain are very useful in understanding their amplitude and phase velocity behavior. Although individual ray arrivals are composed of the superposition of many modes, the resulting waveform is easily understandable from a ray theory point of view. These results show that the influence of crustal velocity gradients is very important in defining the character of *Lg* in shield areas. Standard simplifications of wave propagation using mode approximations may not apply when the maximum amplitude arrival of *Lg* is actually composed of a particular *S* multiple sensitive to a specific velocity gradient within the crust. Indeed, the maximum amplitude wave group of an *Lg* wave will be expected to change with distance as a new crustal multiple dominates. Array observations, such as those used here, are invaluable in deducing the wave propagation characteristics of this complex phase.

From the differences in character of *Lg* between the ARCESS and NORESS regions it is clear that when constructing travel-time curves for *Lg* in a region, to be used for event locations it is critical for accurate distance locations that the characteristic of the *Lg* wave train be known. This ensures that the correct order of reflection is associated with the first detected arrival in *Lg* at each distance and allows identification of depth phases of earthquakes. Azimuth variations in wave train characteristics can also be significant. For example it appears that the *Lg* wave train from events southwest of ARCESS may have character more similar to the one from events near NORESS, with Moho reflections dominating over waves turning in the lower crust. To determine the *Lg* wave pattern in the southwest region however, events from greater distances are needed. Our search of the IMS database did not return any large enough events from this distance and backazimuth range. We conclude that before automatic locations of local and regional events can become reliable, travel-time curves for the phases dominating *Lg* must be

obtained for all azimuths. This is particularly important where *Sn* waves are small and *Lg* onset is used for distance determination.

References

- Azbel, I. Ya., A. F. Buyanov, V. T. Ionkis, N. V. Sharov and V. P. Sharova (1989). Crustal structure of the Kola Peninsula from inversion of deep seismic sounding data. *Tectonophysics*, 162, 87-99.
- Baumgardt, D. R. (1990). Investigation of teleseismic *Lg* blockage and scattering using regional arrays. *Bull. Seism. Soc. Am.*, 80, 2261-2281.
- Behrens, K. S., S. Goldflam, P. Heikkinen, H. Hirschleber, G. Lindquist and C.-E. Lund (1989). Reflection seismic measurements across the Granulite Belt of the POLAR profile in the northern Baltic Shield, Northern Finland. *Tectonophysics*, 162, 101-111.
- Berthelsen, A. and M. Marker (1986). 1.9-1.8 Ga old strike-slip megashears in the Baltic Shield, and their plate tectonic implications. *Tectonophysics*, 128, 163-181.
- Bowman, J. R. and B. L. N. Kennet (1991). Propagation of *Lg* waves in the North Australian craton: Influence of crustal velocity gradients. *Bull. Seism. Soc. Am.*, 81, 592-610.
- Gaál, G. and R. Gorbatshev (1987). An outline of the Precambrian evolution of the Baltic shield. *Precambrian Research*, 35, 15-52.
- Gaál, G., A. Berthelsen, R. Gorbatshev, R. Kesola, M. I. Lehtonen, M. Marker and P. Raase (1989). Structure and composition of the Precambrian crust along the Polar profile in the northern Baltic Shield. *Tectonophysics*, 162, 1-25.
- Galson, G. A. and St. Mueller (1986). An introduction to the European Geotraverse Project: First results and present plans. *Tectonophysics*, 126, 1-30.
- Glaznev, V. N., A. B. Raevsky and N. V. Sharov (1989). A model of the deep structure of the northeastern part of the Baltic Shield based on joint interpretation of seismic, gravity, magnetic and heat flow data. *Tectonophysics*, 162, 151-163.
- Guggisberg, B. and A. Berthelsen (1987). A two-dimensional velocity-model for the lithosphere beneath the Baltic shield and its possible tectonic significance. *Terra Cognita*, 7, 631-638.
- Guggisberg, B., W. Kaminski and C. Prodehl (1991). Crustal Structure of the Fennoscandian Shield: A travelttime interpretation of the long-range FENNOLORA seismic refraction profile. *Tectonophysics*, 195, 105-137.

- Gundem, M. B. (1984). 2-D seismic synthesis of the Oslo Graben, *Cand. Scient. Thesis*, Inst of Geophysics, University of Oslo, Oslo, Norway, 164pp.
- Hansen, R. A., F. Ringdal and P. G. Richards (1990). The stability of RMS Lg measurements and their potential for accurate estimation of the yields of Soviet underground nuclear explosions, *Bull. Seism. Soc. Am.*, 80, 2106-2126.
- Kaneström, R. and K. Haugland (1971). Profile Section 3-4, in *Deep Seismic Sounding in Northern Europe*, A. Vogel, Editor, Swedish Natural Science Research Council, Stockholm, Sweden, 76-91.
- Kozlovsky, Ye. A. (Editor) (1987). *The Superdeep Well of the Kola Peninsula*, Springer-Verlag, Berlin, W-Germany, 558 pp.
- Langston, C. A. (1982). Aspects of Pn and Pg propagation at regional distances, *Bull. Seism. Soc. Am.*, 72, 457-471.
- Lund, C.-E. (1987). Crustal structure along the northern 'FENNOLORA' profile, *Precambrian Research*, 35, 195-206.
- Luosto, U., S. M. Zverev, I. P. Kosminskaya, H. Korhonen (1983). Observations of Fennolora shots on additional line in Finnish Lapland. In: E. Bisztricsany and G. Szeidovitz (editors), *Proceedings of the 17th Assembly of the European Seismological Commission, Budapest, 1980*. Elsevier, Amsterdam, pp. 517-521.
- Luosto, U., E. R. Flueh, C.-E. Lund and Working Group (1989). The crustal structure along the POLAR profile from seismic refraction investigations, *Tectonophysics*, 162, 51-85.
- Mykkeltveit, S. (1980). A seismic profile in Southern Norway, *Pure Appl. Geophys.*, 118, 1310-1325.
- Nuttli, O. W. (1973). Seismic wave attenuation and magnitude relations for Eastern North America, *J. Geophys. Res.*, 78, 876-885.
- Sereno, T. J., S. R. Bratt and T. C. Bache (1988). Simultaneous inversion of regional wave spectra for attenuation and seismic moment in Scandinavia, *J. Geophys. Res.*, 93, 2019-2035.
- Vogfjörd, K. S., 1991. A study of NORESS-array seismograms from local and regional events, *Ph. D. Thesis*, Pennsylvania State University, University Park, 160 pp.
- Vogfjörd, K. S. and C. A. Langston (1991). Analysis of regional events recorded at NORESS, *Bull. Seism. Soc. Am.*, 80, 2016-2031.

Table 1
List of Events recorded at ARCESS

Date	O.T.	Id*	Lat°	Lon°	ML
10/17/1989	11:10:33.05	167198	69.629	30.684	2.50
11/04/1989	10:05:21.28	240323	64.776	30.444	2.70
11/17/1989	12:42:57.85	282554	69.336	30.915	2.72
11/24/1989	16:02:28.82	309164	66.951	21.662	2.35
01/31/1990	12:45:51.20	326360a	69.175	30.772	2.40
01/31/1990	12:47:44.68	326360b	68.990	30.396	2.44
03/07/1990	10:24:51.49	329174	67.615	34.030	3.20
04/12/1990	12:09:06.46	335253	69.208	35.281	2.78
07/26/1990	06:12:31.59	348962	69.533	31.968	2.98
10/19/1990	12:31:46.01	389141	67.618	33.354	2.43
10/26/1990	12:36:08.02	391745	69.446	31.277	2.61
10/31/1990	00:07:48.90	392876	67.954	21.223	2.07
11/06/1990	12:18:20.61	1350700	68.093	32.503	2.49
11/28/1990	12:02:07.10	1356637	64.716	30.362	2.77
12/16/1990	00:58:27.57	1361299	71.108	28.357	2.26
03/07/1991	11:57:42.14	460928	69.681	30.351	2.63
04/13/1991	21:18:33.99	580540	69.310	23.768	2.30
04/26/1991	12:38:57.00	709134a	69.261	30.774	2.20
04/26/1991	12:39:37.00	709134b	69.229	30.710	2.32
05/08/1991	11:56:12.68	760713	69.203	32.175	2.37
06/13/1991	10:48:23.23	905793	67.754	20.156	2.49
07/13/1991	01:42:20.70	981647	67.995	23.862	2.19
07/20/1991	16:53:30.81	998975	70.371	29.338	1.90
08/13/1991	06:57:53.64	1106255	69.583	30.425	2.26
08/24/1991	10:57:35.13	1143047	65.712	32.100	3.18
09/05/1991	15:30:39.71	1206482	67.074	20.954	2.32
09/05/1991	17:07:51.25	1206599	70.376	29.552	1.80
04/24/1992	07:21:30.43	1907025	69.686	30.097	2.25
08/29/1992	22:40:01.96	2621571	67.859	20.682	1.97

* Name of waveform file in the IMS database at CSS.

Table 2
List of Events recorded at NORESS

Date	O.T.	Id	Lat°	Lon°	ML
09/05/1991	17:18:21.05	1205897*	60.273	11.134	1.22
07/17/1992	11:24:09.79	1996500*	60.361	11.213	1.23
11/21/1991	15:15:53.91	1430815*	60.917	11.043	1.34
06/03/1991	15:05:50.00	876819*	60.855	11.048	1.43
06/18/1992	11:02:18.07	2181139*	60.844	10.986	1.09
05/12/1988	17:45:55.90	88133†	61.3	9.5	2.0
09/23/1988	05:46:40.40	88267†	61.1	10.1	2.0
06/07/1988	13:06:14.40	88159†	61.5	8.8	2.1
05/26/1988	11:56:46.80	88147a†	61.2	9.3	2.4
11/11/1988	15:38:27.90	88316†	61.1	10.1	2.1
08/31/1988	12:09:52.60	88244†	60.9	10.7	1.7

* Name of waveform file in the IMS database at CSS.

† Julian date of events obtained from NORESS bulletin at CSS.

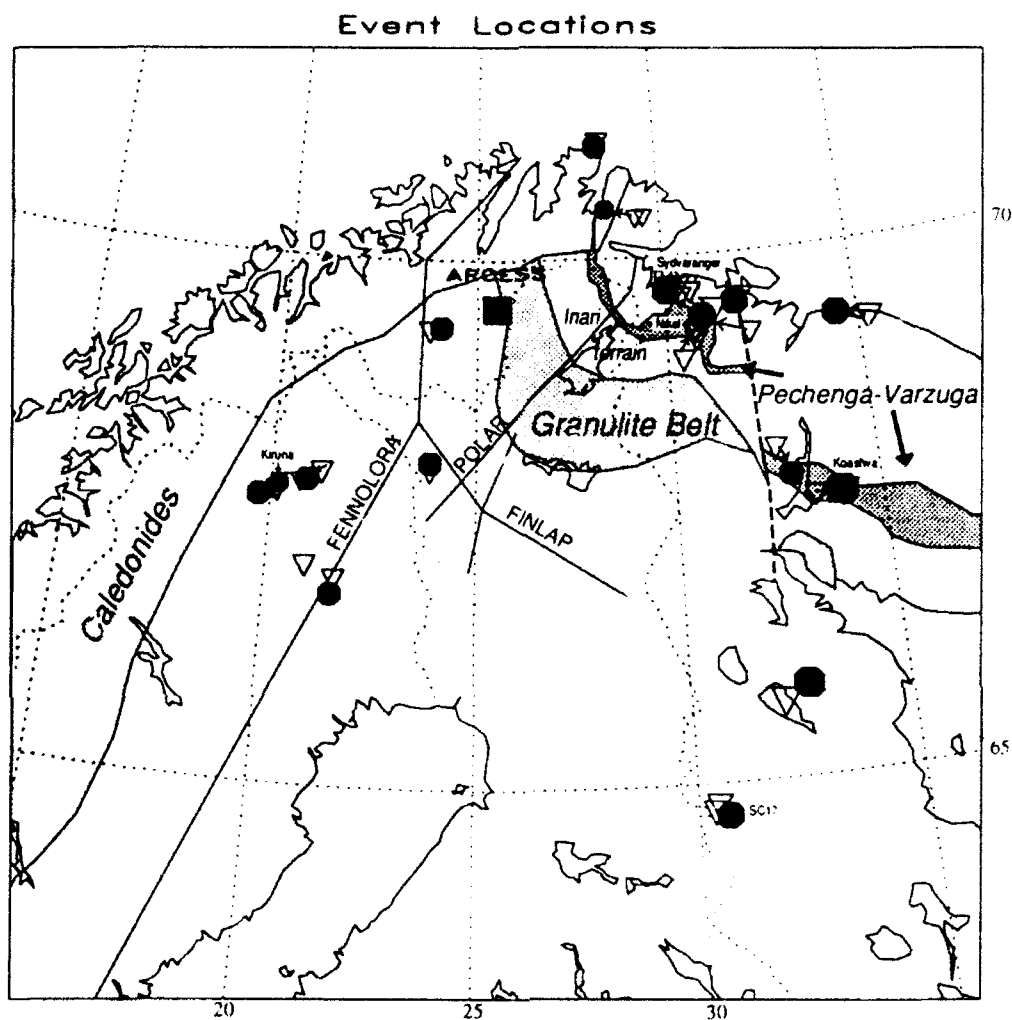


Figure 1. Map showing structural units, and location of ARCESS (square) and events (triangles). Relocated positions are shown with circles. Known mines are indicated. The FENNOLORA, POLAR and FINLAP refraction profiles are also identified.

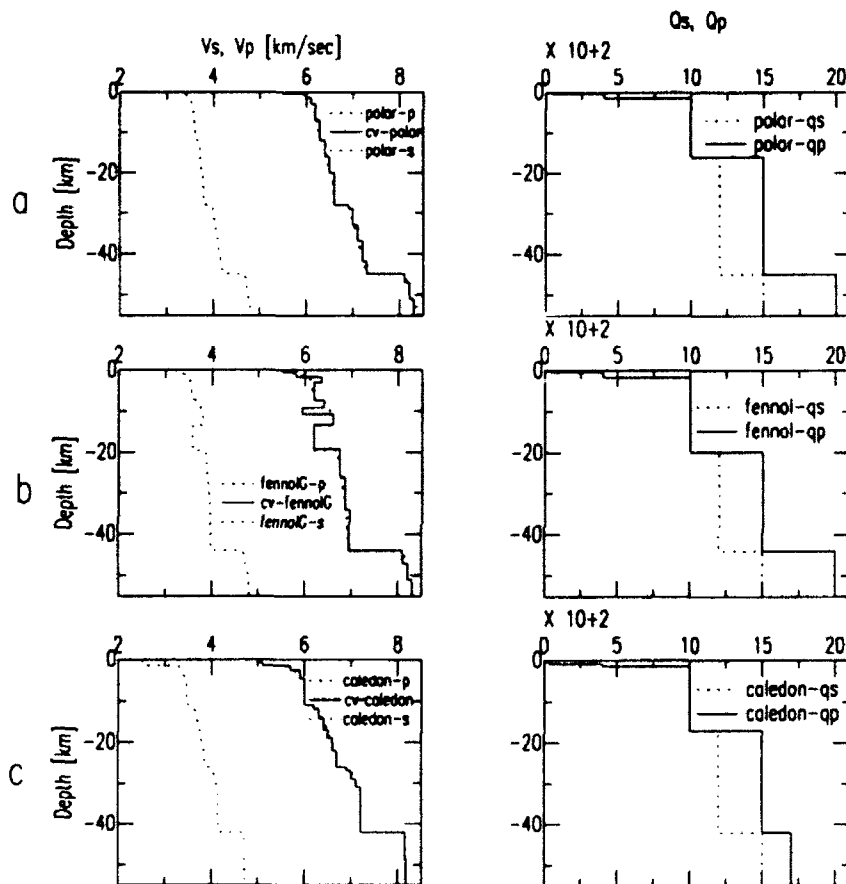


Figure 2. P- and S-wave velocity and Q structure of three crustal and upper mantle models. Gradient velocity models (dashed) are used for travel-time calculations, constant-velocity models (solid) are used for synthetic seismogram calculations. a) Average structure under the northern part of POLAR refraction profile; b) Structure on FENNOLORA, just north of intersection with the FINLAP profile; c) Structure in the Caledonian region northwest of the NORESS array.

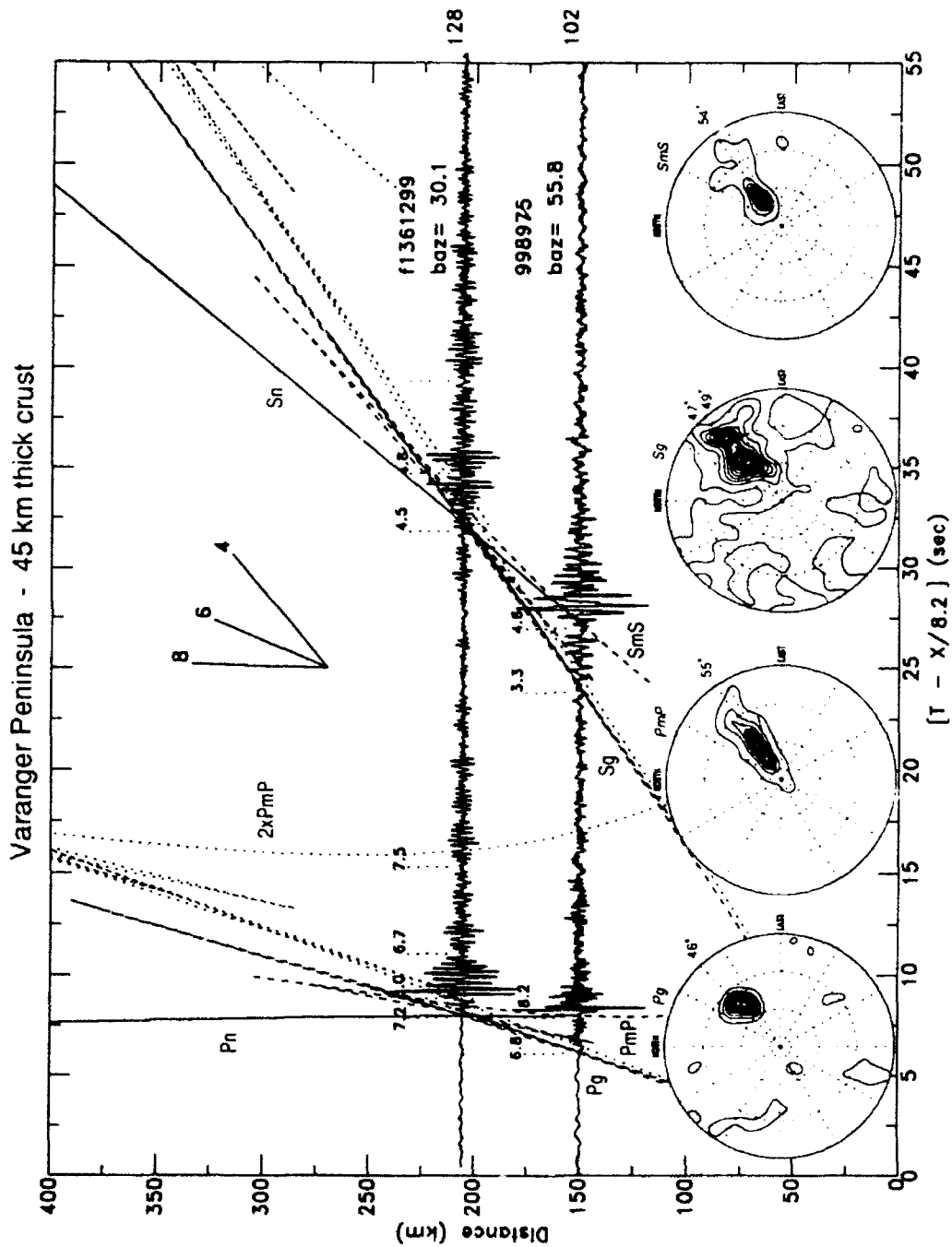


Figure 3. Composite seismogram record section for two events on Varanger Peninsula. Stacking velocities are indicated above each beam section of the composites. Event 1361299 has been high-pass filtered at 1 Hz. Travel-time curves for the main phases are superimposed on the plot. Phase velocities on the travel-time curves can be read from the velocity template in the top center of the plot. Broad-band f-k power plots for the four main phases of event 998975 are plotted at the bottom to show the difference in backazimuth between 1.5 and 5.8 Hz. Maximum horizontal wavenumber is 2.0 1/km.

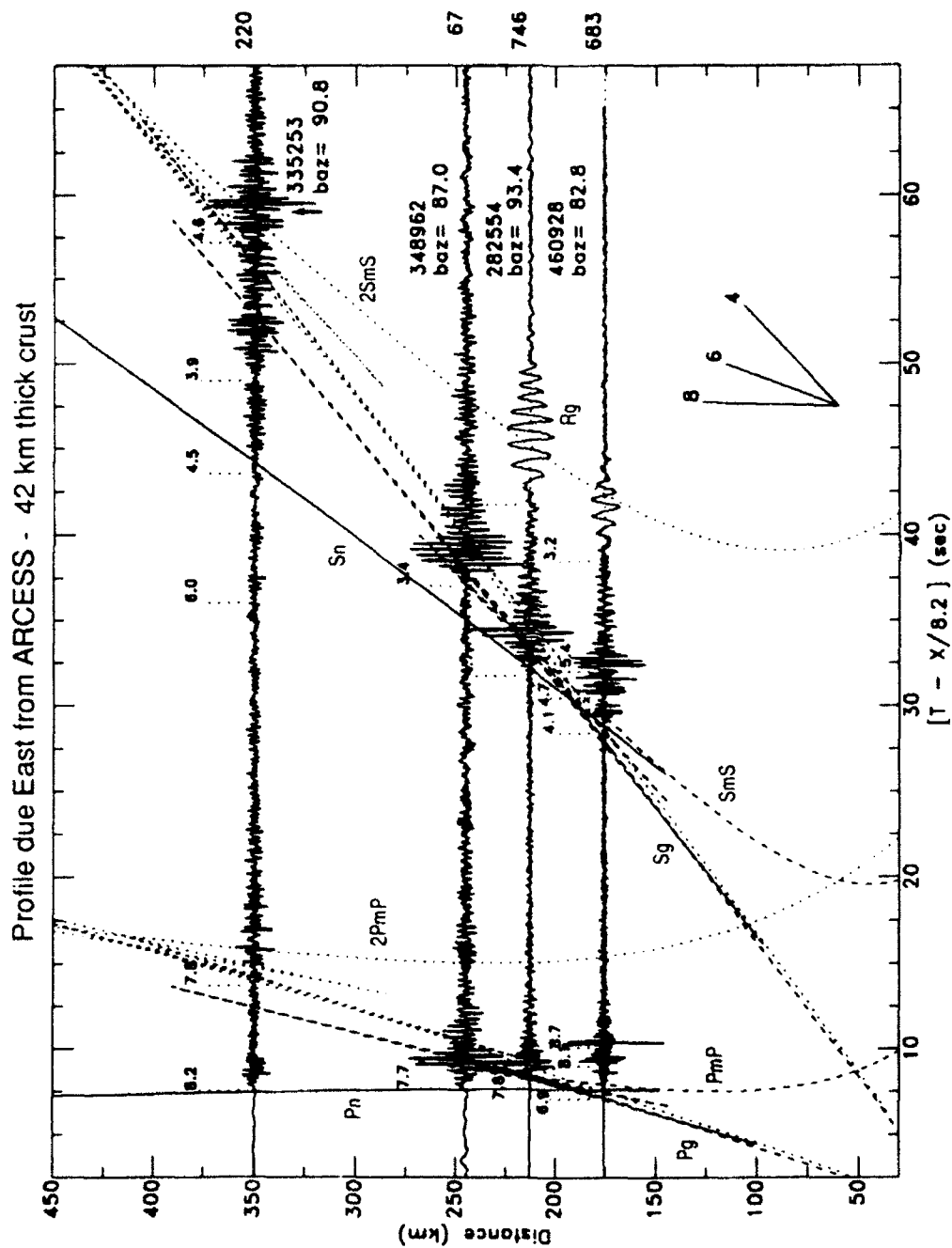


Figure 4. Composite seismogram record section of events located due east of ARCESS. Traces are normalized to maximum amplitude, shown at the end of each trace. Backazimuth and event id are shown above each trace. Travel-time curves of main phases are superimposed. An arrow at 59 sec indicates the Lg time pick of Lg arrival in event 335253.

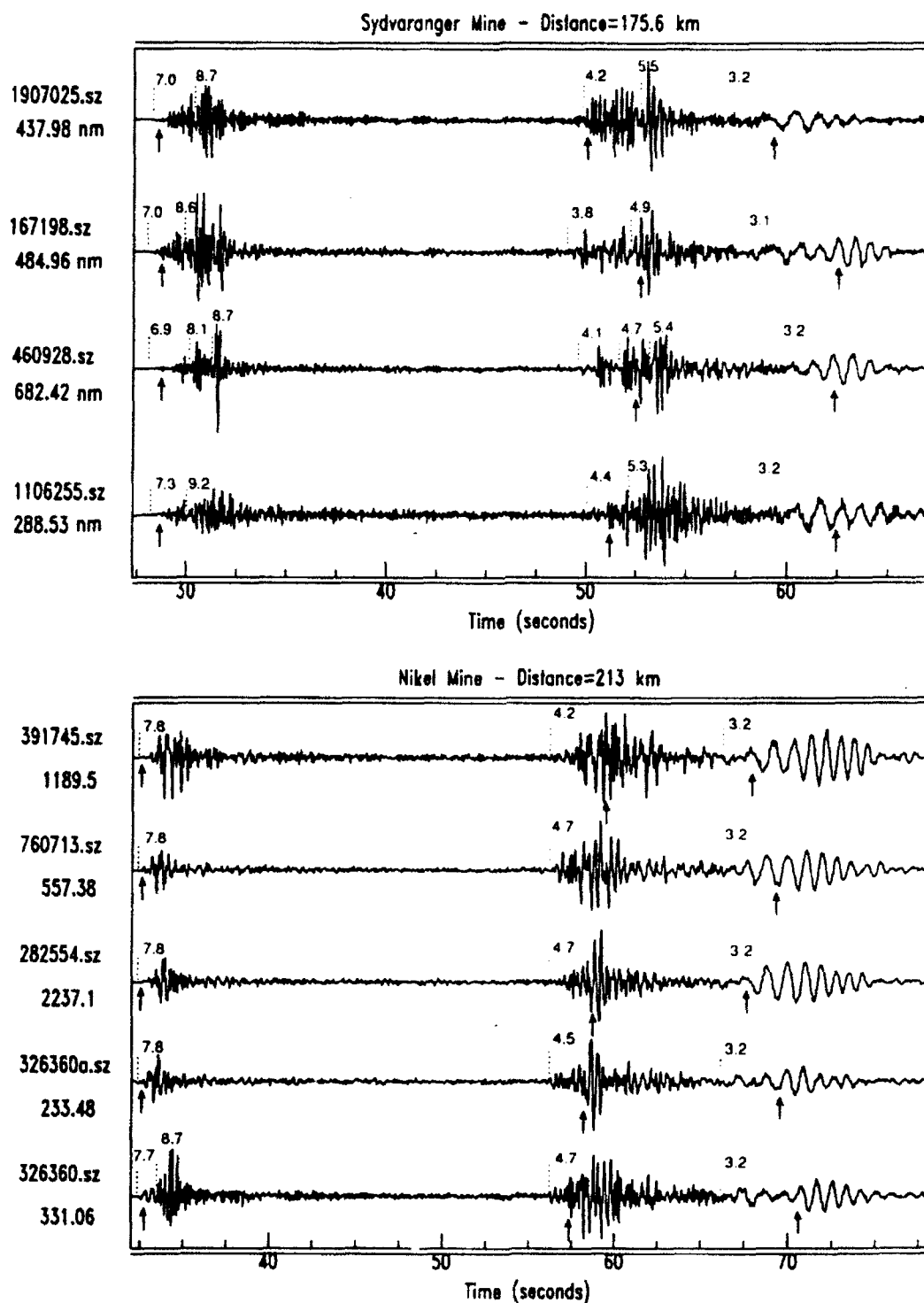


Figure 5. Events from Sydvaranger mine (upper) and Nikel mine (lower) aligned on first arrival. Traces are normalized to maximum amplitude, shown to the left. Stacking velocities are indicated above each beam section. Arrows indicate Pn, Lg and Rg time picks from IMS. Note the multiplicity in some of the events.

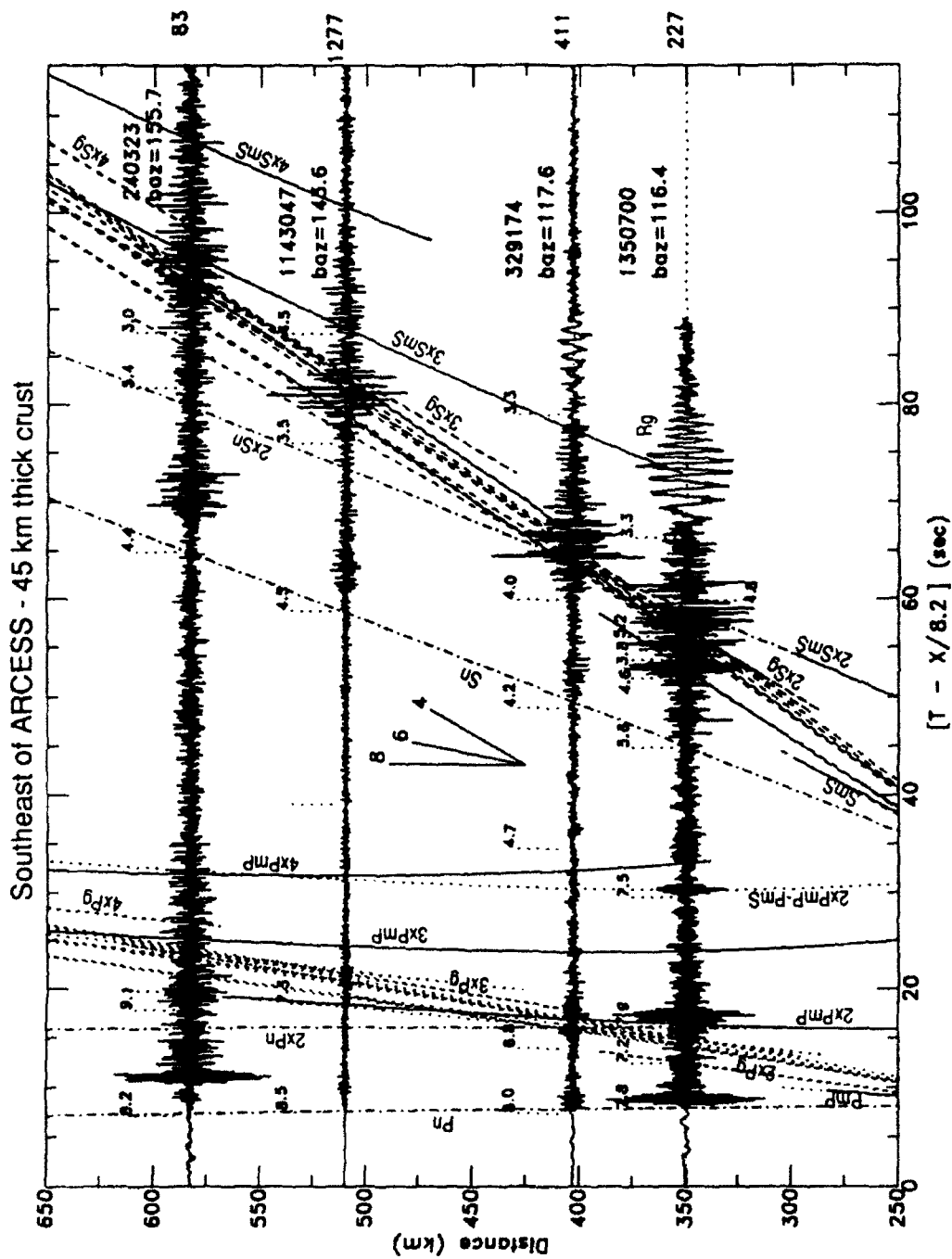


Figure 6. Composite seismogram record section of events located southeast of ARCESS. Travel-time curves for the main phases in the Polar model are superimposed. Rg is observed out to 400 km distance. Pn, Sn and multiples in the Lg wave train, 2xSg, 3xSg, 2xSmS and 3xSmS, dominate in this distance range. The multiple arrivals in the Lg wave train of event 1350700 are probably due to a double explosion.

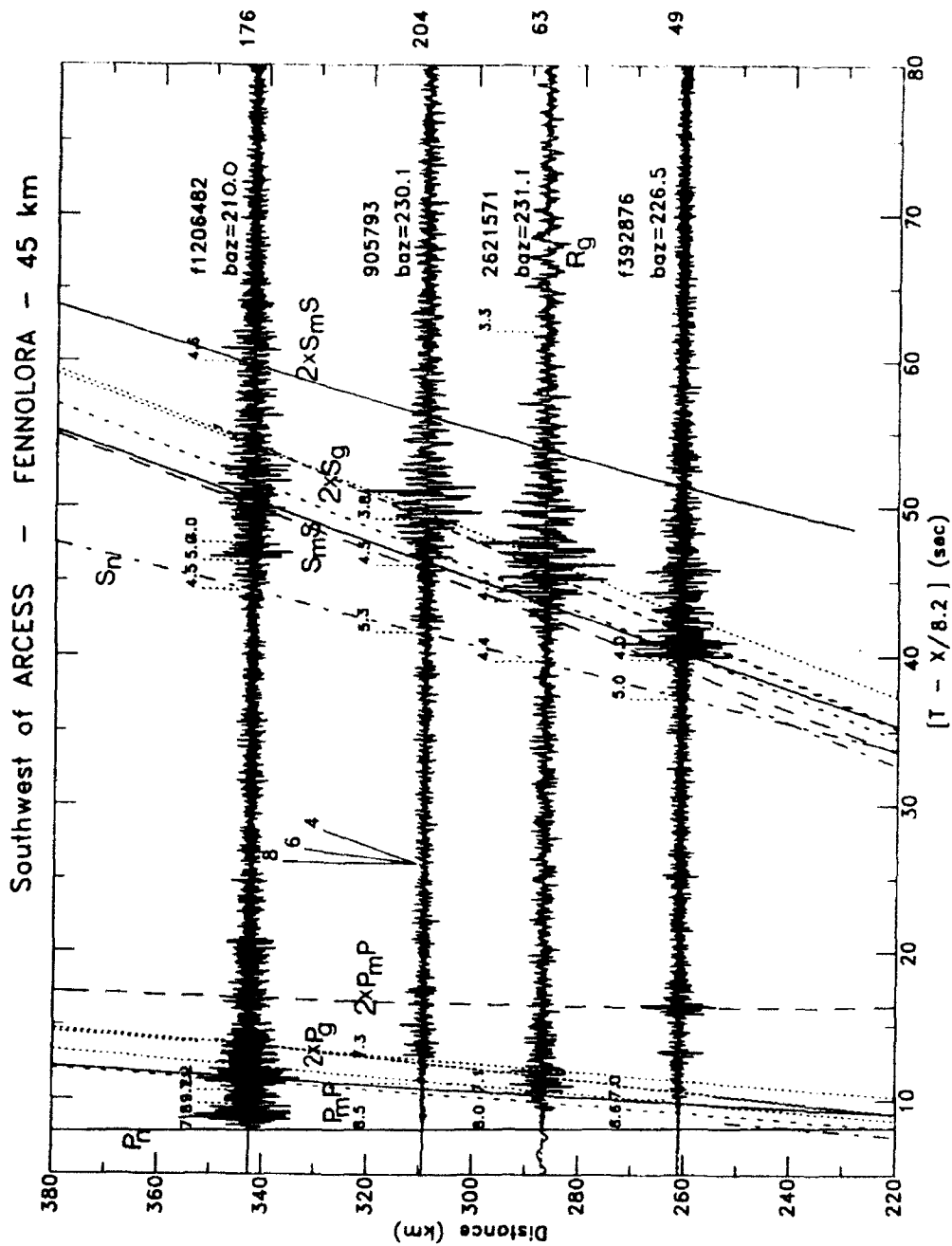


Figure 7. Composite seismogram record section, of events located southwest of ARCESS. Travel-time curves for the main phases in the Fennolora model are superimposed. R_g is only detected in the Kiruna event at 286 km distance. S_m amplitude is decreasing and $2 \times S_g$ increasing between 280 and 310 km. At 340 km distance and 210 backazimuth, however, event 1206482 has large Moho reflections. There are also double arrivals in P_n and S_n from this event.

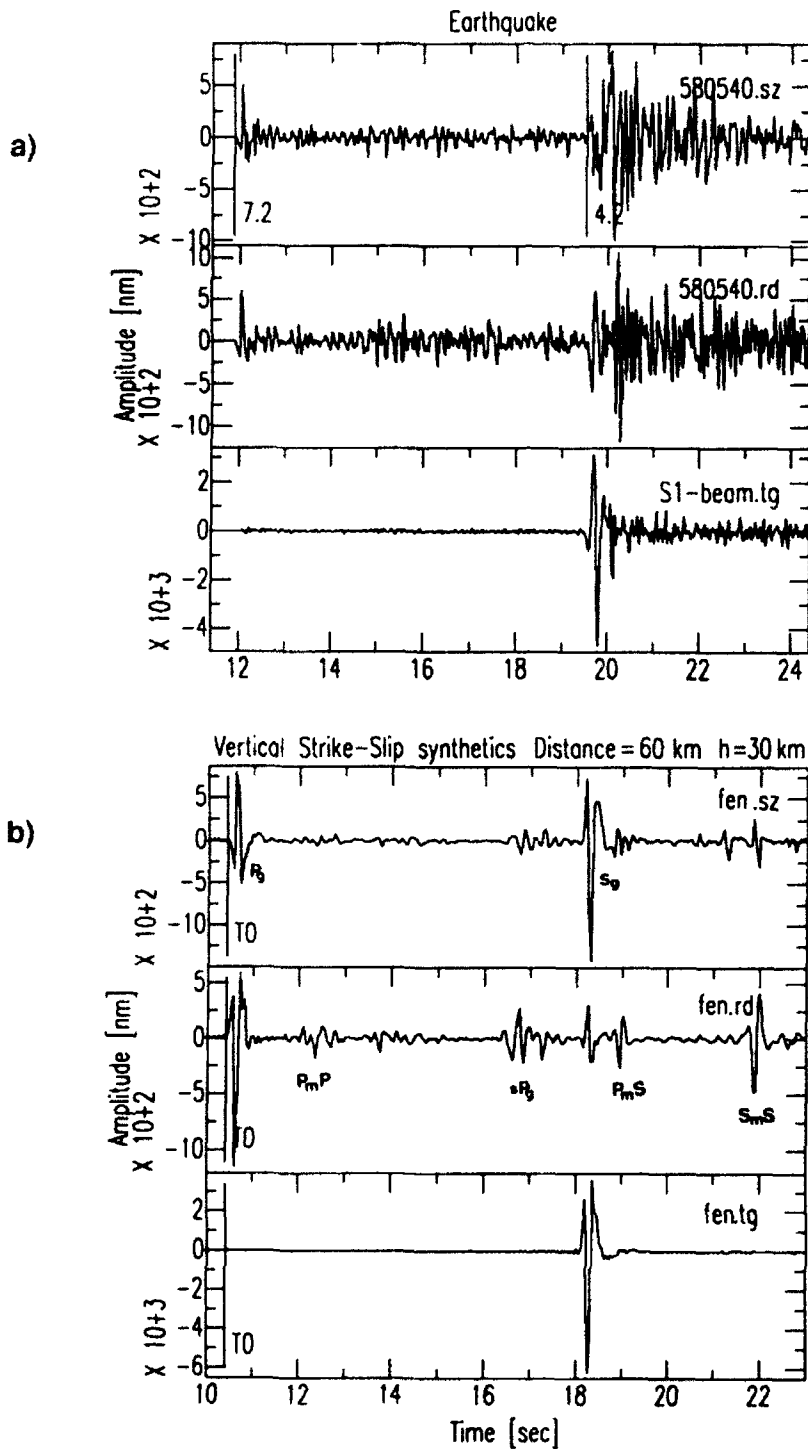


Figure 8. a) Three components (vertical, radial and tangential) of composite seismograms for an event 60 km southwest of ARCESS. The high phase-velocities require the source depth to be around 30 km. b) Three component strike-slip synthetics at 60 km distance in the Fennolara model.

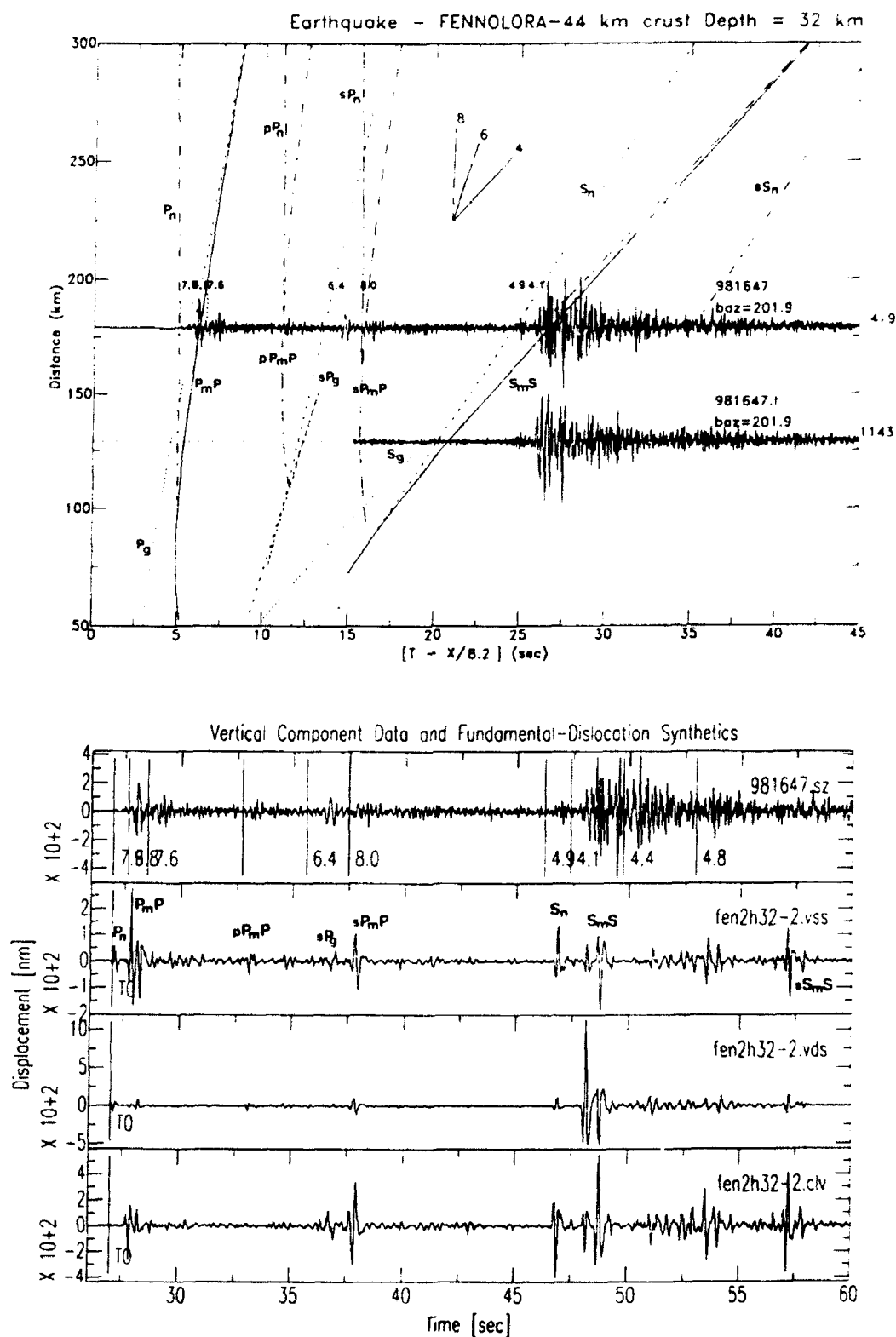


Figure 9. a) Vertical and tangential composite seismograms for event 981647, with travel-time curves calculated for a source at 32 km depth in the Fennolora model. The tangential component is offset in distance to lign up with the vertical. b) Vertical-component synthetics for the three fundamental dislocation sources at 32 km depth and 180 km distance.

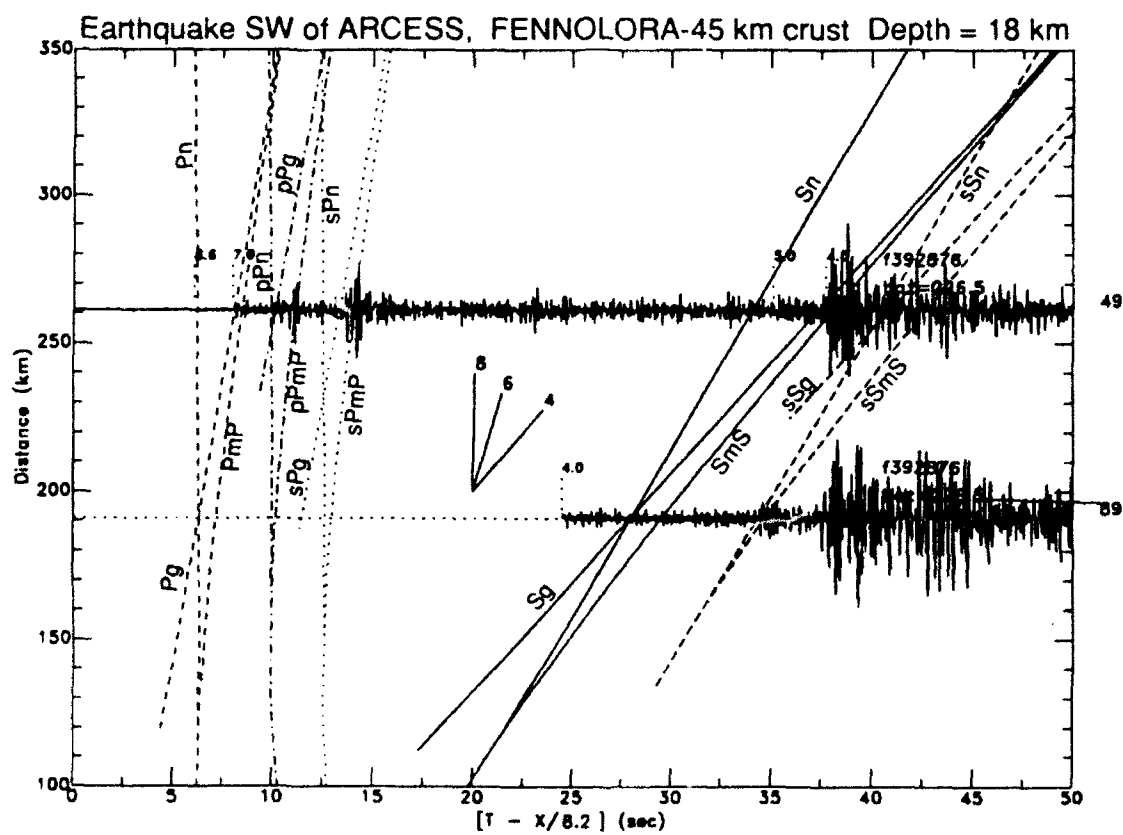


Figure 10. Vertical and horizontal composite seismograms for event 392876 high-passed at 2 Hz. Travel-time curves calculated for a source at 18 km depth in the FennoLogra model are superimposed on the plot. The tangential component is shifted in distance to line up with the vertical component.

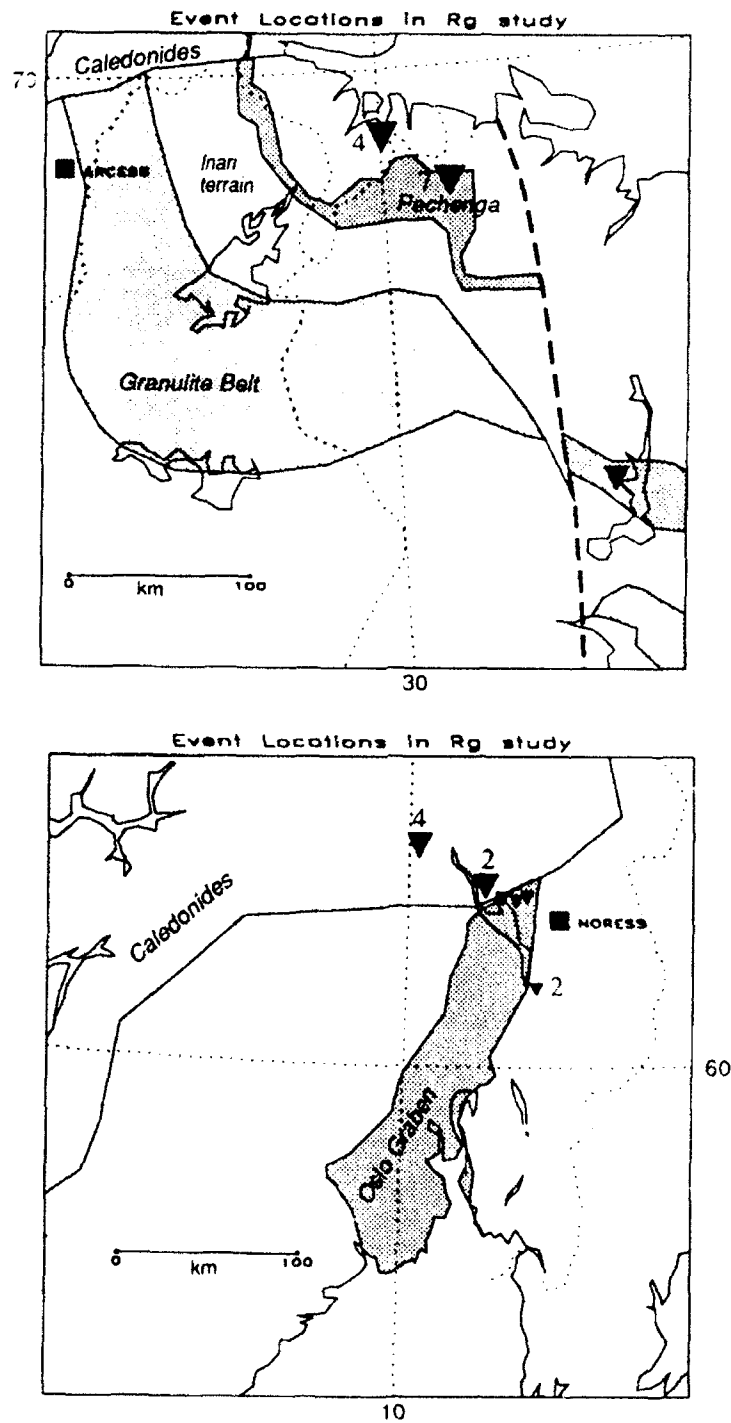


Figure 11. Location of events (triangles) used in Rg study. Locations of arrays are marked by squares.
a) ARCESS region, main structural units are outlined and number of events from each location is indicated;
b) NORESS region, the Permian Oslo Graben and Caledonides are shaded. White area is Precambrian.

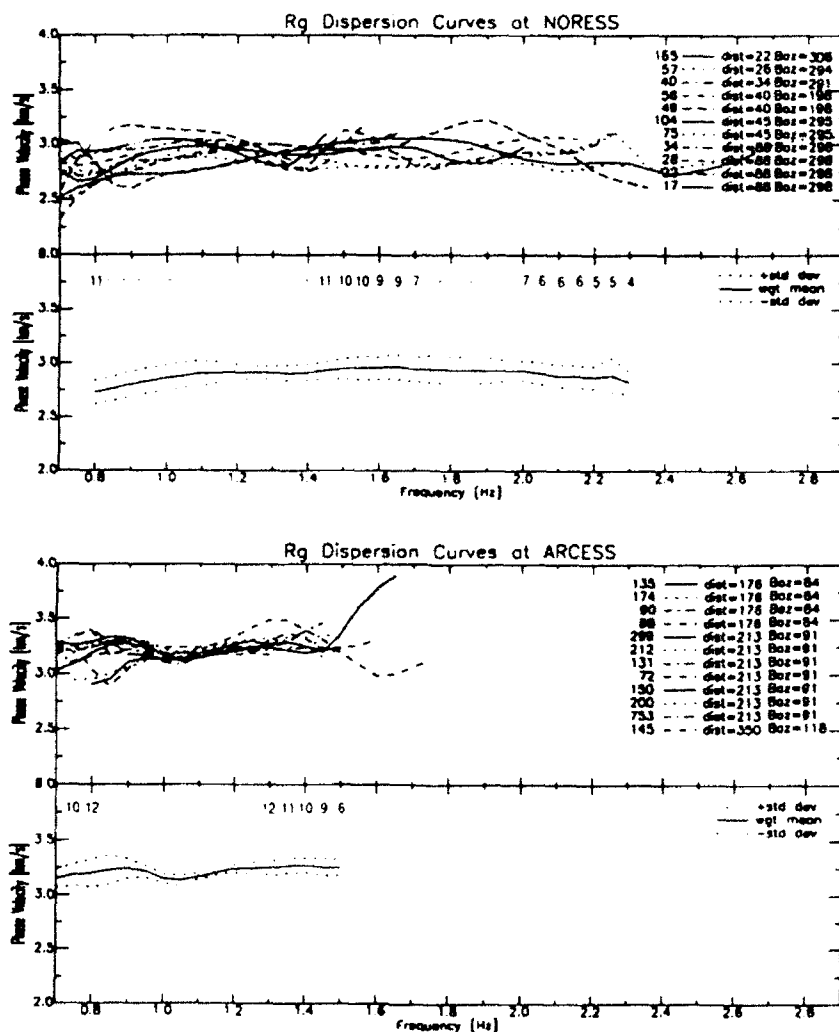
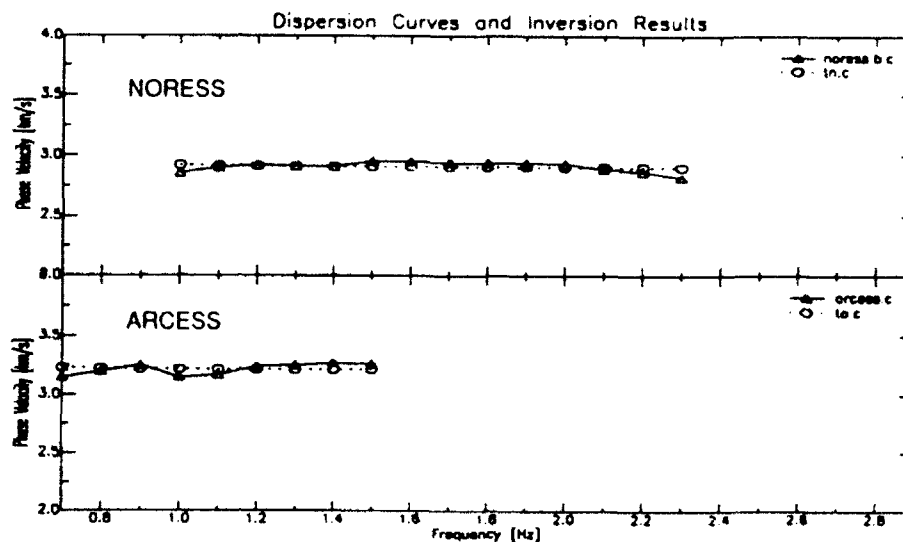


Figure 12. Rg-wave phase-velocity dispersion curves obtained from NORESS (Upper panel) and ARCESS data (lower panel). Weighted mean dispersion curves with one standard deviation limits are plotted below the dispersion curves. The number of samples at each frequency is shown.



NORESS

Layer Thickness [km]	Vs [km/s]	Std. Deviation [km/s]
0.5	3.16	0.09
0.5	3.16	0.07
0.5	3.16	0.10
0.5	3.15	0.14
0.5	3.14	0.18

ARCESS

Layer Thickness [km]	Vs [km/s]	Std. Deviation [km/s]
0.5	3.51	0.14
0.5	3.50	0.10
0.5	3.48	0.09
0.5	3.45	0.13
0.5	3.44	0.17

Figure 13. Fit of the final dispersion curves (circles) obtained from inversions to the weighted mean dispersion curves (triangles) of the data. Inversion results, i.e. S-wave velocities of the layers resolved, for each array are shown below.

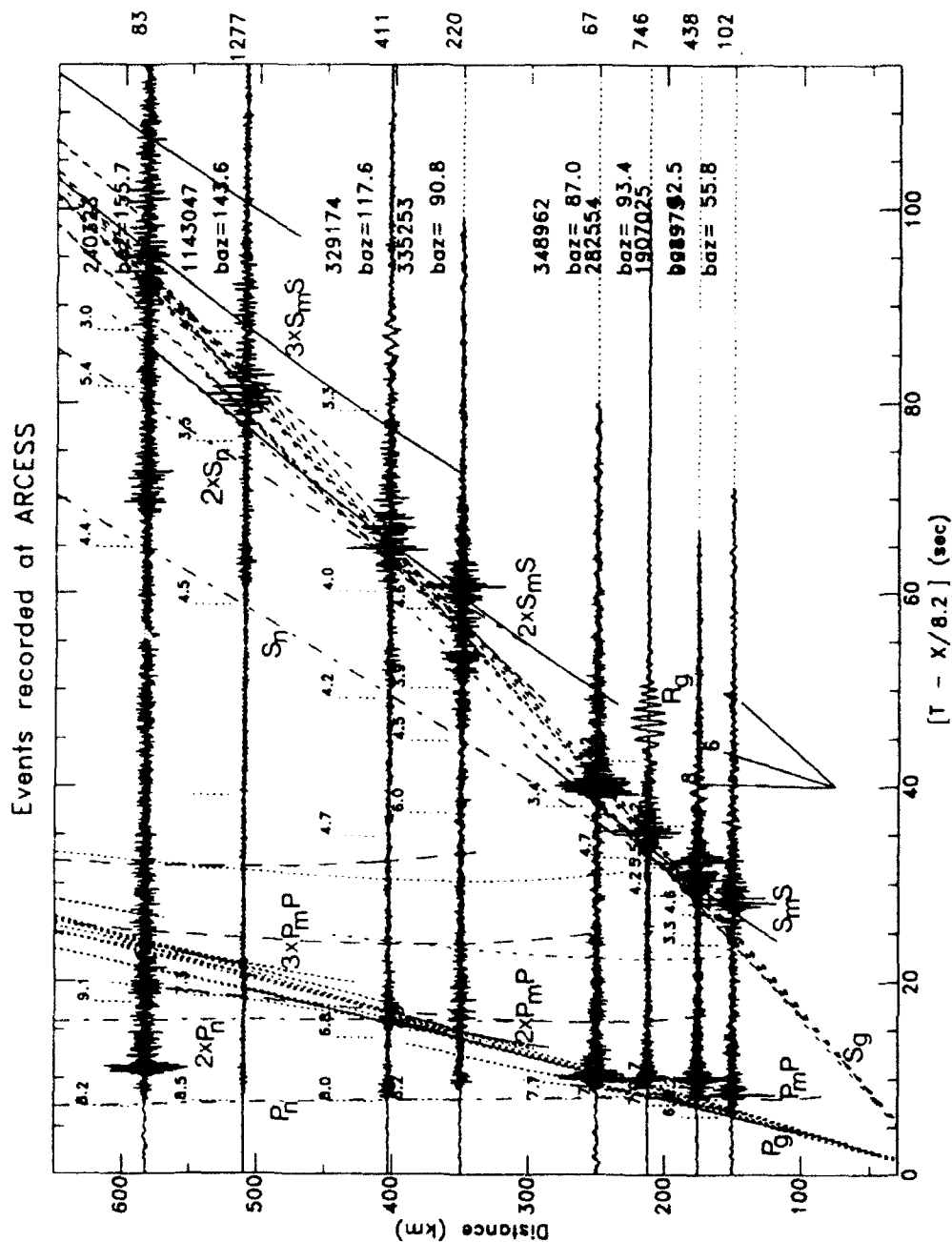


Figure 14. Composite record section of events in the Archean region around ARCESS. Travel-time curves for a 45 km thick Polar model are superimposed on the plot. The record section is dominated by turning waves and Moho reflections. P_n and S_n are also large. Each reflection dominates over a limited distance range. R_g is observed to 400 km distance.

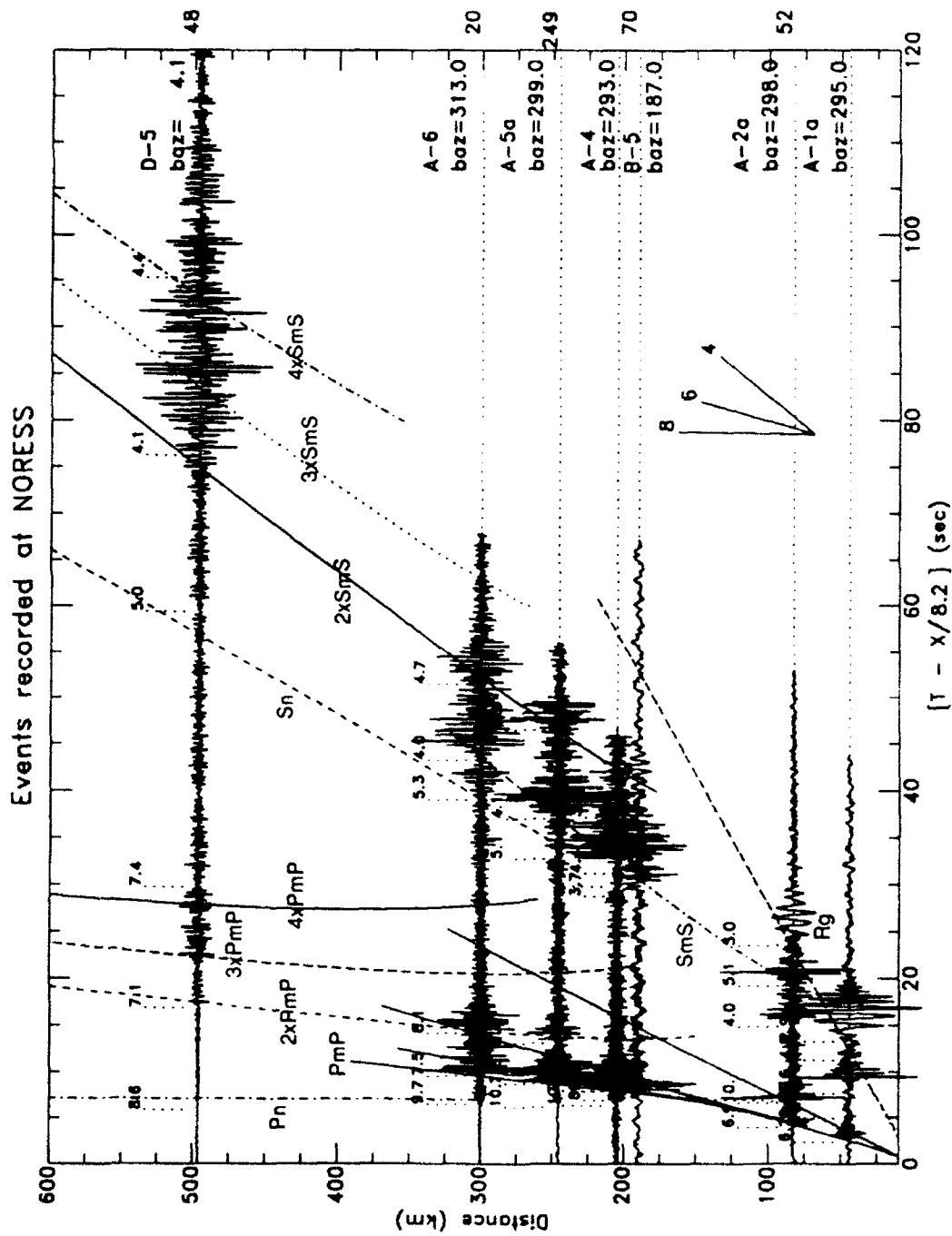


Figure 15. Composite seismograms for events located in the Caledonian region northwest of NORESS. Travel-time curves are calculated for a near surface source in the Caledon model, with a 36 km thick crust. The record section is dominated by Moho reflections. The first reflection dominates out to 300 km, where the second multiple has also become large. At 500 km the second to fourth multiples in the Lg wave train dominate the seismogram. Upper mantle waves, Pn and Sn are small.

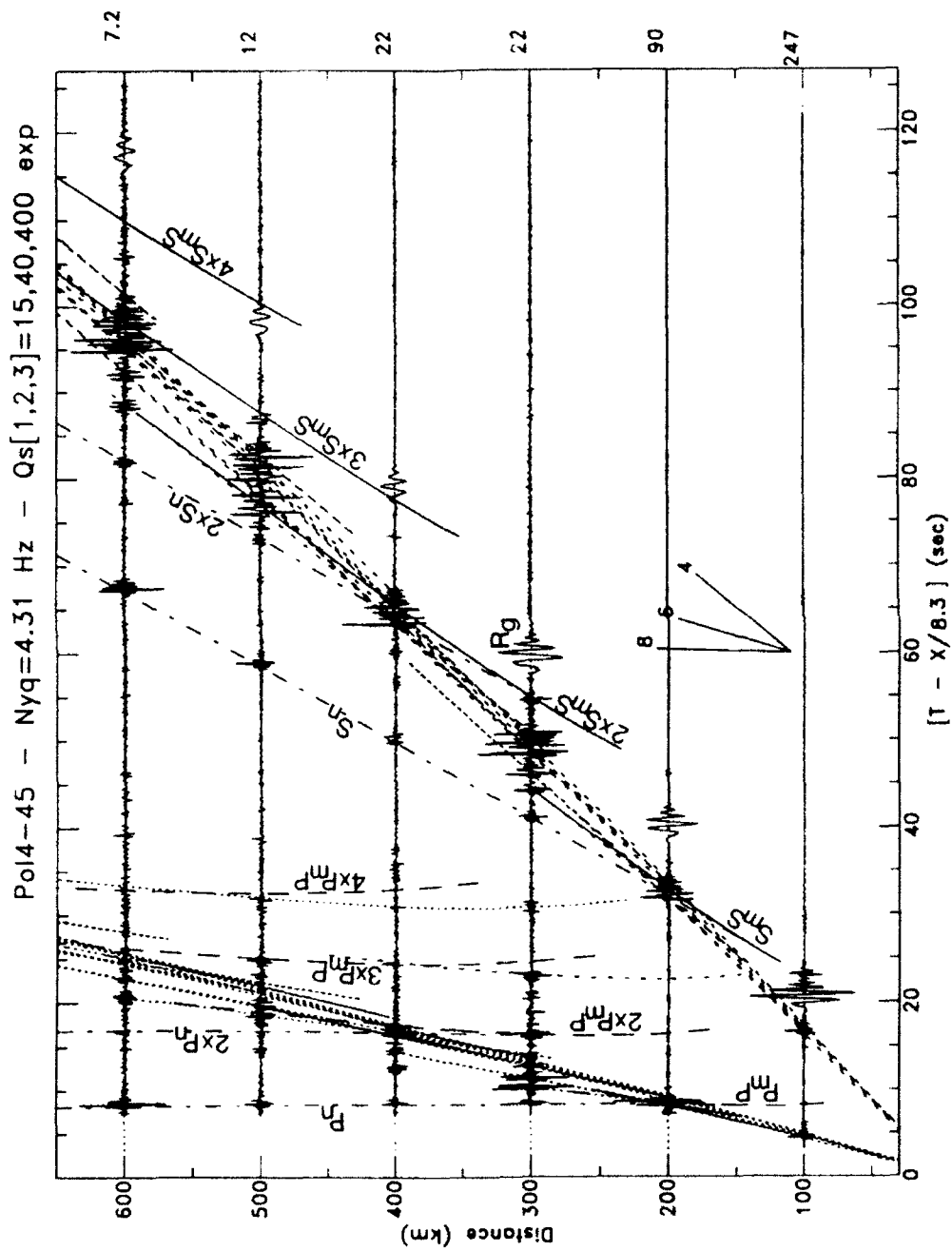


Figure 16. Synthetic-seismogram record section, of an explosion source at 0.1 km depth in the Polar model of Figure 2a. Travel-time curves are superimposed on the plot. The record section is dominated by turning waves and Moho reflections in the Lg wave train. Crustal P-waves diminish quickly with distance, while Rg-wave amplitudes are significant over the whole profile. Upper mantle waves, P_n and S_n , are also large.

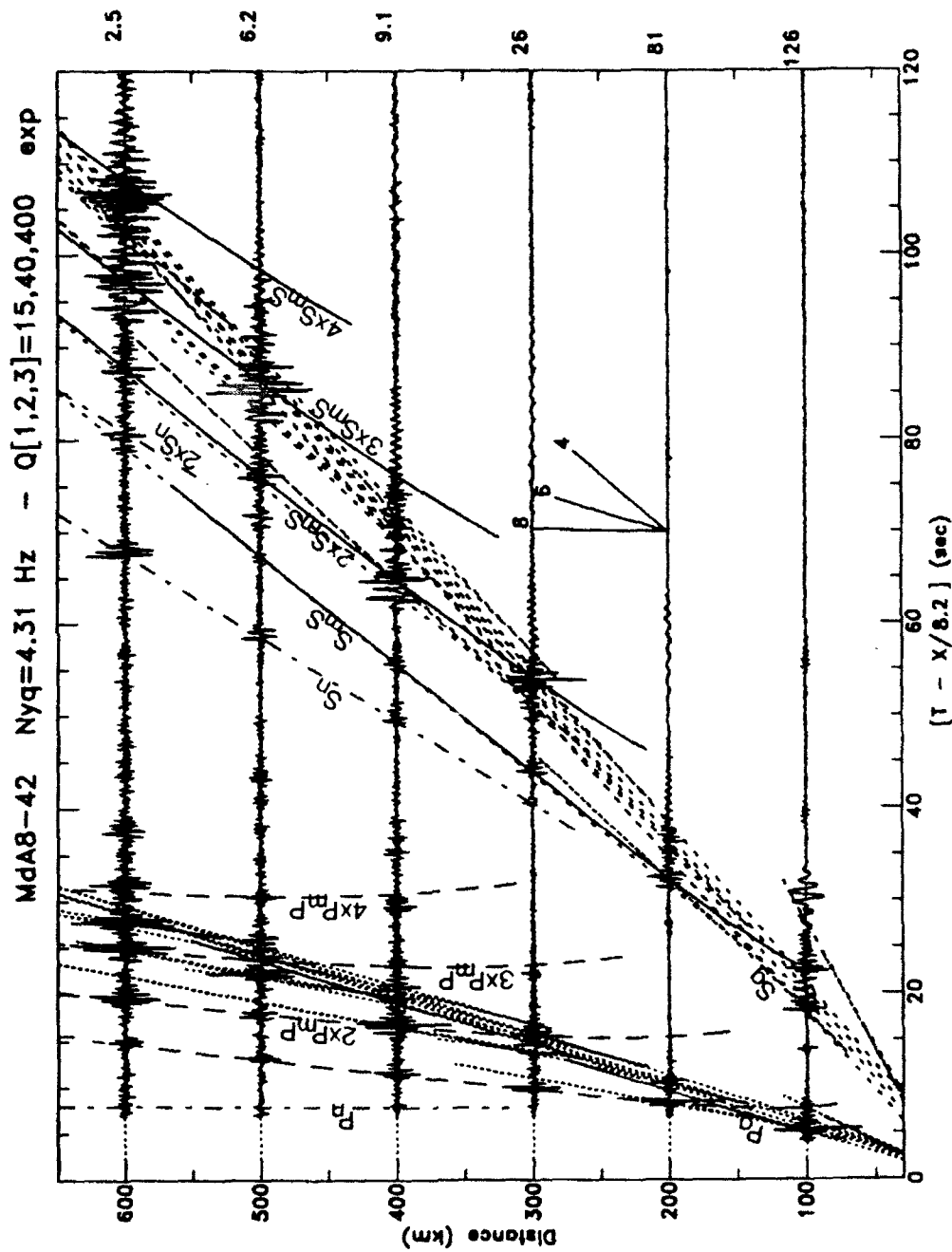


Figure 17. Synthetic-seismogram record section, of an explosion source at 0.1 km depth in the Caledon model of Figure 2c. Travel-time curves are superimposed on the plot. The record section is dominated by Moho reflections in the crustal P and Lg wave trains. Each reflection can be traced over a greater distance than in the Polar model and the number of reverberations increases with distance. Rg does not propagate past 200 km. Pn is small, but Sn is of significant amplitude.

Prof. Thomas Ahrens
Seismological Lab, 252-21
Division of Geological & Planetary Sciences
California Institute of Technology
Pasadena, CA 91125

Prof. Keiiti Aki
Center for Earth Sciences
University of Southern California
University Park
Los Angeles, CA 90089-0741

Prof. Shelton Alexander
Geosciences Department
403 Deike Building
The Pennsylvania State University
University Park, PA 16802

Dr. Ralph Alewine, III
DARPA/NMRO
3701 North Fairfax Drive
Arlington, VA 22203-1714

Prof. Charles B. Archambeau
CIRES
University of Colorado
Boulder, CO 80309

Dr. Thomas C. Bache, Jr.
Science Applications Int'l Corp.
10260 Campus Point Drive
San Diego, CA 92121 (2 copies)

Prof. Muawia Barazangi
Institute for the Study of the Continent
Cornell University
Ithaca, NY 14853

Dr. Jeff Barker
Department of Geological Sciences
State University of New York
at Binghamton
Vestal, NY 13901

Dr. Douglas R. Baumgardt
ENSCO, Inc
5400 Port Royal Road
Springfield, VA 22151-2388

Dr. Susan Beck
Department of Geosciences
Building #77
University of Arizona
Tucson, AZ 85721

Dr. T.J. Bennett
S-CUBED
A Division of Maxwell Laboratories
11800 Sunrise Valley Drive, Suite 1212
Reston, VA 22091

Dr. Robert Blandford
AFTAC/IT, Center for Seismic Studies
1300 North 17th Street
Suite 1450
Arlington, VA 22209-2308

Dr. Stephen Bratt
Center for Seismic Studies
1300 North 17th Street
Suite 1450
Arlington, VA 22209-2308

Dr. Lawrence Burdick
IGPP, A-025
Scripps Institute of Oceanography
University of California, San Diego
La Jolla, CA 92093

Dr. Robert Burrige
Schlumberger-Doll Research Center
Old Quarry Road
Ridgefield, CT 06877

Dr. Jerry Carter
Center for Seismic Studies
1300 North 17th Street
Suite 1450
Arlington, VA 22209-2308

Dr. Eric Chael
Division 9241
Sandia Laboratory
Albuquerque, NM 87185

Dr. Martin Chapman
Department of Geological Sciences
Virginia Polytechnical Institute
21044 Derring Hall
Blacksburg, VA 24061

Prof. Vernon F. Cormier
Department of Geology & Geophysics
U-45, Room 207
University of Connecticut
Storrs, CT 06268

Prof. Steven Day
Department of Geological Sciences
San Diego State University
San Diego, CA 92182

Marvin Denny
U.S. Department of Energy
Office of Arms Control
Washington, DC 20585

Dr. Zoltan Der
ENSCO, Inc.
5400 Port Royal Road
Springfield, VA 22151-2388

Prof. Adam Dziewonski
Hoffman Laboratory, Harvard University
Dept. of Earth Atmos. & Planetary Sciences
20 Oxford Street
Cambridge, MA 02138

Prof. John Ebel
Department of Geology & Geophysics
Boston College
Chestnut Hill, MA 02167

Eric Fielding
SNEE Hall
INSTOC
Cornell University
Ithaca, NY 14853

Dr. Mark D. Fisk
Mission Research Corporation
735 State Street
P.O. Drawer 719
Santa Barbara, CA 93102

Prof Stanley Flatte
Applied Sciences Building
University of California, Santa Cruz
Santa Cruz, CA 95064

Dr. John Foley
NER-Geo Sciences
1100 Crown Colony Drive
Quincy, MA 02169

Prof. Donald Forsyth
Department of Geological Sciences
Brown University
Providence, RI 02912

Dr. Art Frankel
U.S. Geological Survey
922 National Center
Reston, VA 22092

Dr. Cliff Frolich
Institute of Geophysics
8701 North Mopac
Austin, TX 78759

Dr. Holly Given
IGPP, A-025
Scripps Institute of Oceanography
University of California, San Diego
La Jolla, CA 92093

Dr. Jeffrey W. Given
SAIC
10260 Campus Point Drive
San Diego, CA 92121

Dr. Dale Glover
Defense Intelligence Agency
ATTN: ODT-1B
Washington, DC 20301

Dr. Indra Gupta
Teledyne Geotech
314 Montgomery Street
Alexandria, VA 22314

Dan N. Hagedorn
Pacific Northwest Laboratories
Battelle Boulevard
Richland, WA 99352

Dr. James Hannon
Lawrence Livermore National Laboratory
P.O. Box 808
L-205
Livermore, CA 94550

Dr. Roger Hansen
HQ AFTAC/TTR
130 South Highway A1A
Patrick AFB, FL 32925-3002

Prof. David G. Harkrider
Seismological Laboratory
Division of Geological & Planetary Sciences
California Institute of Technology
Pasadena, CA 91125

Prof. Danny Harvey
CIRES
University of Colorado
Boulder, CO 80309

Prof. Donald V. Helmberger
Seismological Laboratory
Division of Geological & Planetary Sciences
California Institute of Technology
Pasadena, CA 91125

• Prof. Eugene Herrin
Institute for the Study of Earth and Man
Geophysical Laboratory
Southern Methodist University
Dallas, TX 75275

• Prof. Robert B. Herrmann
Department of Earth & Atmospheric Sciences
St. Louis University
St. Louis, MO 63156

Prof. Lane R. Johnson
Seismographic Station
University of California
Berkeley, CA 94720

Prof. Thomas H. Jordan
Department of Earth, Atmospheric &
Planetary Sciences
Massachusetts Institute of Technology
Cambridge, MA 02139

Prof. Alan Kafka
Department of Geology & Geophysics
Boston College
Chestnut Hill, MA 02167

Robert C. Kemerait
ENSCO, Inc.
445 Pineda Court
Melbourne, FL 32940

Dr. Karl Koch
Institute for the Study of Earth and Man
Geophysical Laboratory
Southern Methodist University
Dallas, Tx 75275

• Dr. Max Koontz
U.S. Dept. of Energy/DP 5
Forrestal Building
• 1000 Independence Avenue
Washington, DC 20585

Dr. Richard LaCoss
MIT Lincoln Laboratory, M-200B
P.O. Box 73
Lexington, MA 02173-0073

Dr. Fred K. Lamb
University of Illinois at Urbana-Champaign
Department of Physics
1110 West Green Street
Urbana, IL 61801

Prof. Charles A. Langston
Geosciences Department
403 Deike Building
The Pennsylvania State University
University Park, PA 16802

Jim Lawson, Chief Geophysicist
Oklahoma Geological Survey
Oklahoma Geophysical Observatory
P.O. Box 8
Leonard, OK 74043-0008

Prof. Thorne Lay
Institute of Tectonics
Earth Science Board
University of California, Santa Cruz
Santa Cruz, CA 95064

Dr. William Leith
U.S. Geological Survey
Mail Stop 928
Reston, VA 22092

Mr. James F. Lewkowicz
Phillips Laboratory/GPEH
29 Randolph Road
Hanscom AFB, MA 01731-3010(2 copies)

Mr. Alfred Lieberman
ACDA/VI-OA State Department Building
Room 5726
320-21st Street, NW
Washington, DC 20451

Prof. L. Timothy Long
School of Geophysical Sciences
Georgia Institute of Technology
Atlanta, GA 30332

Dr. Randolph Martin, III
New England Research, Inc.
76 Olcott Drive
White River Junction, VT 05001

Dr. Robert Masse
Denver Federal Building
Box 25046, Mail Stop 967
Denver, CO 80225

Dr. Gary McCartor
Department of Physics
Southern Methodist University
Dallas, TX 75275

Prof. Thomas V. McEvilly
Seismographic Station
University of California
Berkeley, CA 94720

Dr. Art McGarr
U.S. Geological Survey
Mail Stop 977
U.S. Geological Survey
Menlo Park, CA 94025

Dr. Keith L. McLaughlin
S-CUBED
A Division of Maxwell Laboratory
P.O. Box 1620
La Jolla, CA 92038-1620

Stephen Miller & Dr. Alexander Florence
SRI International
333 Ravenswood Avenue
Box AF 116
Menlo Park, CA 94025-3493

Prof. Bernard Minster
IGPP, A-025
Scripps Institute of Oceanography
University of California, San Diego
La Jolla, CA 92093

Prof. Brian J. Mitchell
Department of Earth & Atmospheric Sciences
St. Louis University
St. Louis, MO 63156

Mr. Jack Murphy
S-CUBED
A Division of Maxwell Laboratory
11800 Sunrise Valley Drive, Suite 1212
Reston, VA 22091 (2 Copies)

Dr. Keith K. Nakanishi
Lawrence Livermore National Laboratory
L-025
P.O. Box 808
Livermore, CA 94550

Dr. Carl Newton
Los Alamos National Laboratory
P.O. Box 1663
Mail Stop C335, Group ESS-3
Los Alamos, NM 87545

Dr. Bao Nguyen
HQ AFTAC/ITR
130 South Highway A1A
Patrick AFB, FL 32925-3002

Prof. John A. Orcutt
IGPP, A-025
Scripps Institute of Oceanography
University of California, San Diego
La Jolla, CA 92093

Prof. Jeffrey Park
Kline Geology Laboratory
P.O. Box 6666
New Haven, CT 06511-8130

Dr. Howard Patton
Lawrence Livermore National Laboratory
L-025
P.O. Box 808
Livermore, CA 94550

Dr. Frank Pilotte
HQ AFTAC/TT
130 South Highway A1A
Patrick AFB, FL 32925-3002

Dr. Jay J. Pulli
Radix Systems, Inc.
201 Perry Parkway
Gaithersburg, MD 20877

Dr. Robert Reinke
ATTN: FCTVTD
Field Command
Defense Nuclear Agency
Kirtland AFB, NM 87115

Prof. Paul G. Richards
Lamont-Doherty Geological Observatory
of Columbia University
Palisades, NY 10964

Mr. Wilmer Rivers
Teledyne Geotech
314 Montgomery Street
Alexandria, VA 22314

Dr. George Rothe
HQ AFTAC/TTR
130 South Highway A1A
Patrick AFB, FL 32925-3002

Dr. Alan S. Ryall, Jr.
DARPA/NMRO
3701 North Fairfax Drive
Arlington, VA 22209-1714

Dr. Richard Sailor
TASC, Inc.
55 Walkers Brook Drive
Reading, MA 01867

Prof. Charles G. Sammis
Center for Earth Sciences
University of Southern California
University Park
Los Angeles, CA 90089-0741

Prof. Christopher H. Scholz
Lamont-Doherty Geological Observatory
of Columbia University
Palisades, NY 10964

Dr. Susan Schwartz
Institute of Tectonics
1156 High Street
Santa Cruz, CA 95064

Secretary of the Air Force
(SAFRD)
Washington, DC 20330

Office of the Secretary of Defense
DDR&E
Washington, DC 20330

Thomas J. Sereno, Jr.
Science Application Int'l Corp.
10260 Campus Point Drive
San Diego, CA 92121

Dr. Michael Shore
Defense Nuclear Agency/SPSS
6801 Telegraph Road
Alexandria, VA 22310

Dr. Robert Shumway
University of California Davis
Division of Statistics
Davis, CA 95616

Dr. Matthew Sibol
Virginia Tech
Seismological Observatory
4044 Derring Hall
Blacksburg, VA 24061-0420

Prof. David G. Simpson
IRIS, Inc.
1616 North Fort Myer Drive
Suite 1050
Arlington, VA 22209

Donald L. Springer
Lawrence Livermore National Laboratory
L-025
P.O. Box 808
Livermore, CA 94550

Dr. Jeffrey Stevens
S-CUBED
A Division of Maxwell Laboratory
P.O. Box 1620
La Jolla, CA 92038-1620

Lt. Col. Jim Stobie
ATTN: AFOSR/NL
110 Duncan Avenue
Bolling AFB
Washington, DC 20332-0001

Prof. Brian Stump
Institute for the Study of Earth & Man
Geophysical Laboratory
Southern Methodist University
Dallas, TX 75275

Prof. Jeremiah Sullivan
University of Illinois at Urbana-Champaign
Department of Physics
1110 West Green Street
Urbana, IL 61801

Prof. L. Sykes
Lamont-Doherty Geological Observatory
of Columbia University
Palisades, NY 10964

Dr. David Taylor
ENSCO, Inc.
445 Pineda Court
Melbourne, FL 32940

Dr. Steven R. Taylor
Los Alamos National Laboratory
P.O. Box 1663
Mail Stop C335
Los Alamos, NM 87545

Prof. Clifford Thurber
University of Wisconsin-Madison
Department of Geology & Geophysics
1215 West Dayton Street
Madison, WI 53706

Prof. M. Nafi Toksoz
Earth Resources Lab
Massachusetts Institute of Technology
42 Carleton Street
Cambridge, MA 02142

Dr. Larry Turnbull
CIA-OSWR/NED
Washington, DC 20505

Dr. Gregory van der Vink
IRIS, Inc.
1616 North Fort Myer Drive
Suite 1050
Arlington, VA 22209

Dr. Karl Veith
EG&G
5211 Auth Road
Suite 240
Suitland, MD 20746

Prof. Terry C. Wallace
Department of Geosciences
Building #77
University of Arizona
Tucson, AZ 85721

Dr. Thomas Weaver
Los Alamos National Laboratory
P.O. Box 1663
Mail Stop C335
Los Alamos, NM 87545

Dr. William Wortman
Mission Research Corporation
8560 Cinderbed Road
Suite 700
Newington, VA 22122

Prof. Francis T. Wu
Department of Geological Sciences
State University of New York
at Binghamton
Vestal, NY 13901

AFTAC/CA
(STINFO)
Patrick AFB, FL 32925-6001

DARPA/PM
3701 North Fairfax Drive
Arlington, VA 22203-1714

DARPA/RMO/RETRIEVAL
3701 North Fairfax Drive
Arlington, VA 22203-1714

DARPA/RMO/SECURITY OFFICE
3701 North Fairfax Drive
Arlington, VA 22203-1714

HQ DNA
ATTN: Technical Library
Washington, DC 20305

Defense Intelligence Agency
Directorate for Scientific & Technical Intelligence
ATTN: DTIB
Washington, DC 20340-6158

Defense Technical Information Center
Cameron Station
Alexandria, VA 22314 (2 Copies)

TACTEC
Battelle Memorial Institute
505 King Avenue
Columbus, OH 43201 (Final Report)

Phillips Laboratory
ATTN: XPG
29 Randolph Road
Hanscom AFB, MA 01731-3010

Phillips Laboratory
ATTN: GPE
29 Randolph Road
Hanscom AFB, MA 01731-3010

Phillips Laboratory
ATTN: TSML
5 Wright Street
Hanscom AFB, MA 01731-3004

Phillips Laboratory
ATTN: PL/SUL
3550 Aberdeen Ave SE
Kirtland, NM 87117-5776 (2 copies)

Dr. Svein Mykkeltveit
NTNT/NORSAR
P.O. Box 51
N-2007 Kjeller, NORWAY (3 Copies)

Dr. Michel Bouchon
I.R.I.G.M.-B.P. 68
38402 St. Martin D'Heres
Cedex, FRANCE

Prof. Keith Priestley
University of Cambridge
Bullard Labs, Dept. of Earth Sciences
Madingley Rise, Madingley Road
Cambridge CB3 0EZ, ENGLAND

Dr. Michel Campillo
Observatoire de Grenoble
I.R.I.G.M.-B.P. 53
38041 Grenoble, FRANCE

Dr. Jorg Schlittenhardt
Federal Institute for Geosciences & Nat'l Res.
Postfach 510153
D-3000 Hannover 51, GERMANY

Dr. Kin Yip Chun
Geophysics Division
Physics Department
University of Toronto
Ontario, CANADA

Dr. Johannes Schweitzer
Institute of Geophysics
Ruhr University/Bochum
P.O. Box 1102148
4360 Bochum 1, GERMANY

Prof. Hans-Peter Harjes
Institute for Geophysics
Ruhr University/Bochum
P.O. Box 102148
4630 Bochum 1, GERMANY

Trust & Verify
VERTIC
8 John Adam Street
London WC2N 6EZ, ENGLAND

Prof. Eystein Husebye
NTNF/NORSAR
P.O. Box 51
N-2007 Kjeller, NORWAY

David Jepsen
Acting Head, Nuclear Monitoring Section
Bureau of Mineral Resources
Geology and Geophysics
G.P.O. Box 378, Canberra, AUSTRALIA

Ms. Eva Johannisson
Senior Research Officer
FOA
S-172 90 Sundbyberg, SWEDEN

Dr. Peter Marshall
Procurement Executive
Ministry of Defense
Blacknest, Brimpton
Reading FG7-FRS, UNITED KINGDOM

Dr. Bernard Massinon, Dr. Pierre Mechler
Societe Radiomana
27 rue Claude Bernard
75005 Paris, FRANCE (2 Copies)